Dissertation

Fast and Accurate Identification of Hidden Conductive 3D Objects with Deterministic and Stochastic Methods

Dipl.-Ing. Alice Reinbacher-Köstinger

Institute for Fundamentals and Theory in Electrical Engineering
Graz University of Technology

Supervisor: ao. Univ.-Prof. Dipl.-Ing. Dr. techn. Christian Magele

Graz, February 2011

Abstract

By exploitation of eddy current effects, hidden conductive objects can be detected in principle. A particular challenge is posed by the task of exactly recognizing the position of an object known in shape while hidden by low or non-conductive material. Therefore, excitation coils are used to produce a time harmonic magnetic field and the total magnetic field is measured by magnetic field sensors. The total field is the sum of the excitation field and the field caused by eddy currents in a conductive object. The measured magnetic field depends on the current object position and thus information about the location is available in principle.

Finding the unknown object location parameters for measured magnetic field values is a classic inverse problem. Deterministic as well as stochastic methods can be used basically, nevertheless, convergence speed and global optimization behavior must be considered. While deterministic algorithms converge faster in general, stochastic methods are able to find the global solution and therefore an appropriate combination needs to be found to provide accuracy as well as low identification time.

In this work the developed simulation model and a suitable approximation method for a fast computation of the forward problem is described. The sensitivity of several sensor configurations was investigated to map parameter changes as well as possible to the measurement values. Finally, results due to the identification of the object parameters by a deterministic, a stochastic and a hybrid method are presented.

Kurzfassung

Ist ein elektrisch leitfähiges Objekt zwar in seiner Form bekannt, jedoch von nicht- oder schwach leitfähigem Material umgeben, können Wirbelstromverfahren zur Identifikation der Lage eingesetzt werden. Zu diesem Zweck werden Spulen zur Erzeugung eines Erregerfeldes und Magnetfeldsensoren zur Messung des Gesamtfeldes verwendet. Das Gesamtfeld setzt sich aus dem Erregerfeld und dem Feld des Objektes (erzeugt durch Wirbelströme) zusammen und ändert sich bei unterschiedlichen Objektpositionen und -ausrichtungen.

Das Rückschließen von den gemessenen Daten auf die Objekt-Lageparameter ist ein klassisches nichtlineares, schlechtgestelltes inverses Problem, das mit geeigneten Verfahren gelöst werden muss. Sowohl deterministische als auch stochastische Verfahren können grundsätzlich verwendet werden. Dabei steht die hohe Geschwindigkeit der deterministischen Verfahren dem globalen Verhalten der stochastischen Verfahren gegenüber. Sind beide Eigenschaften gefordert, muss eine geeignete Kombination der Methoden gefunden werden.

In dieser Arbeit werden das Simulationsmodell und eine geeignete Approximationsmethode zur schnellen Berechnung des Vorwärtsproblems, das die Grundlage zur Lösung des inversen Problems darstellt, beschrieben. Mit Hilfe des Vorwärtsproblemlösers wurde die Sensitivität bei unterschiedlichen Sensorkonfigurationen untersucht, um Parameteränderungen so gut wie möglich in den Sensoren erfassen zu können. Schließlich werden die Ergebnisse der Anwendung je eines deterministischen und eines stochastischen Optimierungsverfahrens und einer Hybrid-Variante zur Identifikation der Objektparameter gezeigt.

Statutory Declaration

I declare that I have authored this thesis independently, that I have not used other than the declared sources / resources, and that I have explicitly marked all material which has been quoted either literally or by content from the used sources.

Eidesstattliche Erklärung

Ich erkläre an Eides statt, dass ich die vorliegende Arbeit selbstständig verfasst, andere als die angegebenen Quellen/Hilfsmittel nicht benutzt und die den benutzten Quellen wörtlich und inhaltlich entnommene Stellen als solche kenntlich gemacht habe.

Ort	Datum	Unterschrift

Danksagung

Zu allererst möchte ich meinem Betreuer Christian Magele danken. Er hat mich von Beginn an motiviert und hat mit seinen innovativen Ideen immer wieder neue Aspekte und Lösungsvorschläge aufgezeigt.
Werner Renhart danke ich besonders für die Diskussionen und hilfreichen Anregungen, ohne die die Umsetzung der effizienten Methode zum Lösen des Vorwärtsproblems nicht möglich gewesen wäre. An dieser Stelle danke ich auch Mario Bellina für die Generierung der nötigen Simulationsdaten einerseits und für den Gedankenaustausch zu den Zielen und Realisierungsmöglichkeiten des Tibianagel-Projektes andererseits.
Meinen Dank richte ich an alle Mitarbeitern des Instituts für Grundlagen und Theorie der Elektrotechnik, die mir den entsprechenden Rahmen für meine Dissertation gegeben haben. Ohne die persönliche, fachliche und finanzielle Unterstützung, vor allem um an Konferenzen teilnehmen zu können, hätte ich nicht die Möglichkeit zu Diskussionen mit anderen Wissenschaftlern auf meinem Gebiet gehabt.

Meinen Eltern gebührt besonderer Dank, denn sie haben mir durch ihr Verständnis für Bildung und mit ihrer persönlichen und finanziellen Unterstützung den Weg zu dieser Dissertation überhaupt erst ermöglicht. Meiner Schwester danke ich für die Beispielhaftigkeit, mit der sie mir als Technikerin vorangegangen ist - wenngleich auch mit riesengroßen Fußstapfen.

Chronologisch zuletzt, jedoch innerlich an allererster Stelle, gilt mein Dank meinem Mann Martin. Er hat nicht nur unendlich viel Verständnis für nicht gemeinsam verbrachte Stunden aufgebracht, sondern mich auch stets mental gestärkt und mir durch seine Hilfe ermöglicht, mich voll und ganz auf meine wissenschaftliche Arbeit konzentrieren zu können.

Contents

List of Figures

List of Tables

1 Introduction

1.1 Motivation

In modern human medicine fractures of long bones such as femur, tibia and humerus get stabilized and aligned by the use of intra-medullary nails. An intra-medullary nail is a rod mostly made of titanium alloy and being slightly shorter than the fractured bone. This medullary nail gets inserted into the medullary canal of the bone by a surgical intervention. Subsequently the nail needs to be interlocked at both ends with the bone by the use of bolts. For the interlocking the surgeon has to position the drilling equipment exactly in the rotational axis of the pre-drilled hole in the nail. For this purpose image converters, like mobile X-ray apparatus, are used. These image converters are working well for this application, however the surgeon and the patient are exposed to X-ray radiation during the positioning process, this technique is quite expensive and it might not be available under certain circumstances. The objective of this work is to demonstrate the feasibility of an alternative technique to localize the drill holes by means of eddy current methods which features the required accuracy while being less contaminating, moreover less costly and easily on hand, even in case of natural disaster or in conflict areas.

1.2 Eddy Current Testing Methods

1.2.1 Principle

Alternating currents applied to conductive coils cause an alternating magnetic field. This field is called source field $\mathbf{B}_s$. When conductive materials are exposed to alternating magnetic

fields, eddy currents are developed in the conductive regions. These eddy currents in turn cause a magnetic field $\mathbf{B}_{ec}$, but in opposite direction to the source field (Fig. 1.1).

The total field $\mathbf{B}_t$ can be measured by several magnetic field sensors. A review of magnetic

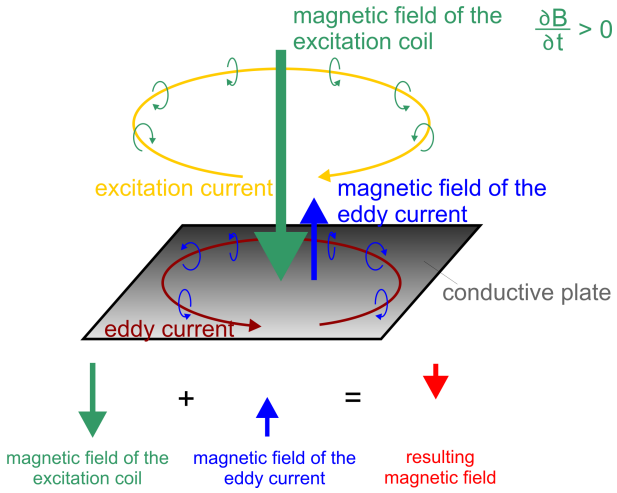

Fig. 1.1: Eddy current principle.

sensors is given in [1]. In many eddy current testing (ECT) applications, e. g. for detecting flaws in conductive material, a relative movement between the object and the sensor is performed. Signal changes can be measured as a function of the sensor position and with this data inferences can be made about cracks or non-conformities in the object. However, to identify an object known in shape but without performing a relative movement, a sufficient number of sensors in an adequate configuration must be used. Suitable sensors for this application are GMR (giant magnetoresistance) sensors that are small, frequency-independent, temperature-stable and cheap. Since GMR sensors are available as PCB devices, the setup of an adequate sensor array is possible for the problem in hand.

1.2.2 Skin Effect

A crucial effect when measuring eddy currents or quantities related to them, is the skin effect. Electromagnetic fields are attenuated when penetrating an electrically conductive material. The attenuation depends on the frequency f, the electric conductivity σ and permeability μ of the material. The principle of the skin effect is shown in Fig. 1.2. The characteristic

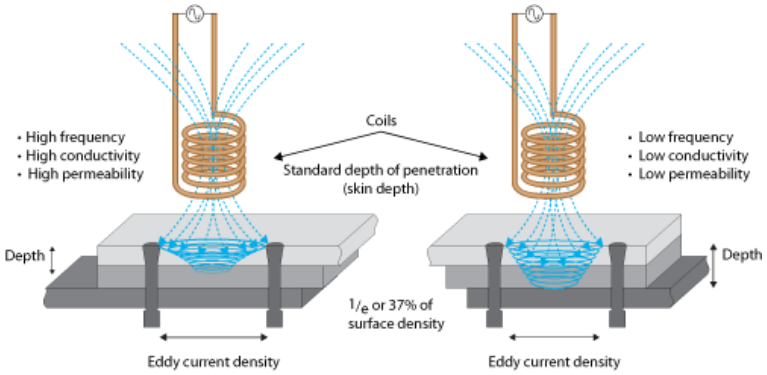

Fig. 1.2: Illustration of the penetration depth in eddy current measurements, [2].

length associated with the decay of the magnetic field to $\frac{1}{e}$ of its original value is called penetration depth δ and can be calculated by (1.1).

$$\delta = \frac{1}{\sqrt{\sigma f \mu \pi}} \tag{1.1}$$

If the penetration depth is too low, inhomogeneities in deeper regions can not be detected. Thus, in addition to medical reasons the choice of the excitation frequency is also dependent on the penetration depth since all other parameters in (1.1) are fixed.

1.3 Preliminary Investigations

1.3.1 Feasibility Studies

In preliminary studies the feasibility to localize inhomogenities in conductive materials with eddy current testing methods were investigated, [3] and [4]. The measurement system was built up by two saddle shaped excitation coils and two receiver coils. The conductive object was positioned anywhere between the two saddle coils and the receiver coils were moved in a defined measurement area, shown in Fig. 1.3. The measurement area is only an illustration of the possible measurement coil positions. This measurement process is a classical non-destructive eddy current testing method.
Analyzing the obtained differential voltages by the gradient coils as a function of the position, the boundary layers between the conductive area of the object and the air were identifiable.

Since the shape of the object is known, the position of the object could be found with the obtained measurements.
In these preliminary studies an object to sensor distance of 3 cm was realized and two degrees of freedom concerning the object position were assumed: the displacement along the rotation axis of the excitation coil system and the rotation about this axis.

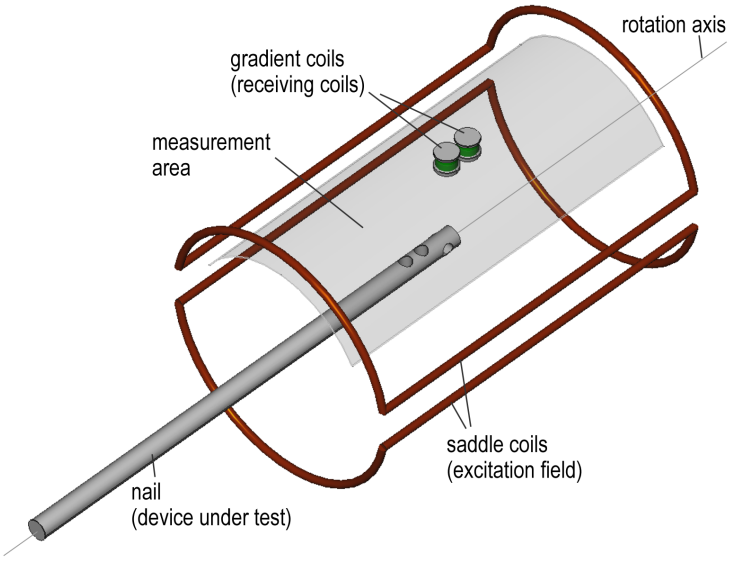

Fig. 1.3: Schematic model of the measurement configuration in [3] and [4].

1.3.2 Improved Sensor System

In [5] magneto resistive sensors, so called giant magnetoresistance sensors, were used instead of gradient coils. On the one hand GMR sensors are the better choice concerning frequency-independence and temperature-stability and on the other hand the tiny structure allows to realize an array of sensors.

1.3.2.1 Giant Magnetoresistance (GMR) Sensors

The principle of GMR sensors is due to the magnetoresistive effect that is the change of the resistivity of a material caused by a magnetic field. In 1986 Peter Grünberg from Jülich Research Center discovered the anti parallel exchange coupling between ferromagnetic layers separated by thin non-ferromagnetic layers. Two years later he discovered the Giant magnetoresistive effect wherefore he got the Nobel Prize in physics in the year 2007. Meanwhile GMR sensors are mainly used in read heads of hard drives and in eddy current testing measurement systems.
GMR sensors are built as printed circuit board assemblies and are accordingly small, very sensitive, stable in temperature, frequency independent and cheap. Most of the sensor types are build up in a Wheatstone bridge configuration to provide temperature compensation [6]. The function between the applied field and the measurable voltage change is linear in a certain range. Fig. 1.4 shows the diagram of a AA-sensor from NVE corporation, which is used in the real test configuration. An appropriate operating point can be reached by providing a direct current flowing beneath the GMR sensors. Details to the biasing method are described in [5]. All GMR magnetic field sensors have a primary axis of sensitivity that is illustrated in Fig. 1.5 and has to be considered in the measurement configuration and, of course, in the simulations. Fig. 1.4 shows the characteristic of three different sensor groups. The sensitivity of the AA002 sensor is declared by 3.0 to 4.2 mV/V/Oe (because of the bridge configuration the sensitivity depends on the source voltage). Assuming a source voltage of 15 V, the sensitivity becomes 0.45 $\frac{\mathrm{mV}}{\mu\mathrm{T}}$ to $\frac{\mathrm{mV}}{\mu\mathrm{T}}$. The intrinsic 1/f noise can be neglected since it tends to zero at the applied excitation frequency of 100 kHz.

1.3.2.2 Measurement System with GMR Sensors

Using a two-dimensional GMR sensor array, magnetic field values were measured in some points in one single measurement configuration. The measurement setup using a GMR array is shown in Fig. 1.6.

The realizations and practical experiences of the preliminary works have shown that the measurement principle, i.e. the eddy current method, is applicable and it is feasible to localize

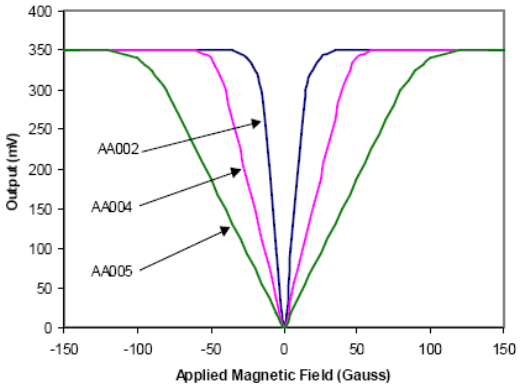

Fig. 1.4: Output of a GMR Wheatstone bridge versus applied field.

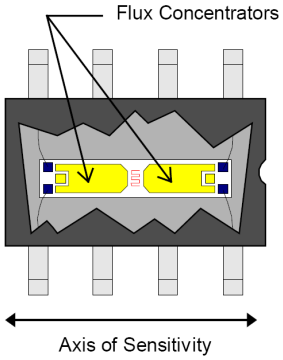

Fig. 1.5: Sensitive magnetic axis of a AA sensor from NVE [6].

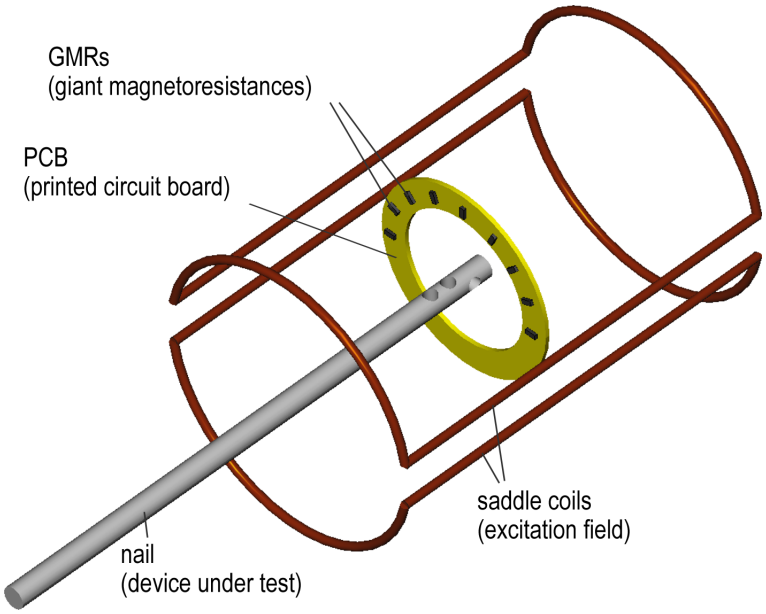

Fig. 1.6: Schematic model of the measurement configuration in [5]. The GMR sensors are mounted on a ring-shaped printed circuit board (PCB).

a conductive object known in shape, even if the distance between the object and the sensors is about 3 cm.

1.4 Aims and Objectives

Starting from the knowledge obtained by practical preliminary investigations, possibilities to identify the position and the orientation of a conductive object known in shape by taking measurements at a single, stationary measurement configuration have to be found. Hence, the inverse problem, i.e. finding the unknown parameters for observed or measured effects in physical systems, has to be solved. Therefore it is necessary to create a simulation model for the measurement system to solve the so called forward problem first. Since inverse problems are in common solved by iterative minimization algorithms where in each iteration the forward problem has to be solved at least one time, the forward problem computation time should be kept as small as possible.
Deterministic as well as stochastic methods can be used to solve the inverse problem. In this work a comparison of both methods should be drawn and a particular method of each type (deterministic and stochastic) should be applied to the inverse eddy current problem in hand. Additionally, combinations of deterministic and stochastic algorithms should be investigated to find an accurate solution in a sufficient time.
Thus, the aims of this work can be summarized as follows:

- Development of a fast numerical forward problem solver.
- Sensitivity analysis of the measurement system using different sensor array configurations.
- Comparing deterministic and stochastic inverse problem solving methods.
- Applying inverse problem solving methods to the object identification problem in hand.
- Determination of the maximum allowed measurement data noise level to achieve a sufficient identification accuracy.

1.5 Problem Description

1.5.1 Introduction

A tibia nail is inserted at the proximal end of the tibia near the patella. The medullary cavity, i.e. the cavity inside the bone, is opened there and the nail is inserted by hand as far as possible. Since the medullary cavity is never straight, the remaining part of the nail must be carefully tapped with a hammer to reach the distal end. During this process the tibia nail is deformed and thus the distal drill holes are no longer identifiable sufficiently accurate by geometric determination.
Hence, applying an eddy current measurement system in the region of the distal drill holes should provide information about the position and orientation of the holes. The magnetic field values can be measured near to the surface of the leg, however, in the majority of cases eddy current testing measurements are taken directly on the conductive object surface. Thus, measurements in larger distances are a special challenge because the eddy current field $\mathbf{B}_{ec}$ is already very low since it decreases with the distance by $\frac{1}{r}$.
In this application the hidden object is made of titanium alloy (Ti6AL4V) with an electric conductivity of $\sigma = 58 \cdot 10^4 \frac{\mathrm{A}}{\mathrm{V\,m}}$. It is rod-shaped with a diameter of about 1 cm, a length of about 35 cm (depends on the size of the human tibia) and has 3 drill holes with a diameter of 0.5 cm each. The outermost drill hole is orthogonal to the other two (Fig. 1.7). In Fig. 1.8 an X-ray image of an implanted tibia nail is shown.

The surrounding material, i.e. the bone and the tissue, has a low conductivity of about $\sigma = 0.5 - 10 \frac{\mathrm{A}}{\mathrm{V\,m}}$, which means that there is a ratio of about $1 : 6 \cdot 10^4$ to $1 : 1 \cdot 10^6$ in conductivity between nail and tissue. In fact, the volume of the surrounding material depends on the anatomy of the lower leg but in this work a maximum thickness of 5 cm is assumed. Hence, this assumption defines the geometry of the excitation and sensor system since it has to enclose the lower leg. The sensor system must be placed between the two opposed saddle coils, thus, a distance of 3 cm from the rotation axis to the sensors and 4.5 cm to the excitation coils was defined (Fig. 1.9).

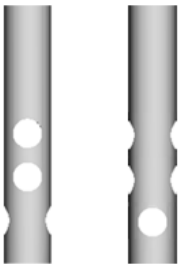

Fig. 1.7: Illustration of the distal drill holes (near to the ankle) of a tibia nail in front and side view.

Fig. 1.8: X-ray image of an implanted tibia nail. The configuration of the drill holes depends on the type of the bone fracture, thus, different nails are used for different injuries.

1.5.2 Measurement Frequency

As described in Section 1.2.2, the choice of the excitation frequency is decisive. Due to the relation between the conductivity, the frequency and the penetration depth given in (1.1), the choice of an appropriate frequency can be made. The diagrams 1.10 and 1.11 show the characteristic of the penetration depth as a function of the frequency for the titanium alloy and the surrounding material.

It can be seen, that the attenuation due to the surrounding material is very small. Assuming, for instance, an excitation frequency of $f = 100\,\mathrm{kHz}$, the penetration depth is about $2.5\,\mathrm{m}$ and therefore it is much bigger than the geometric dimensions of the measurement system. Contrary, the high conductivity of the tibia nail decreases the penetration depth significantly to about $2.5\,\mathrm{mm}$ at the same frequency $f = 100\,\mathrm{kHz}$. Thus, eddy currents are mainly employed on the surface of the nail and hence inhomogeneities are detectable there. Hence, a measurement frequency of $f = 100\,\mathrm{kHz}$ was chosen.

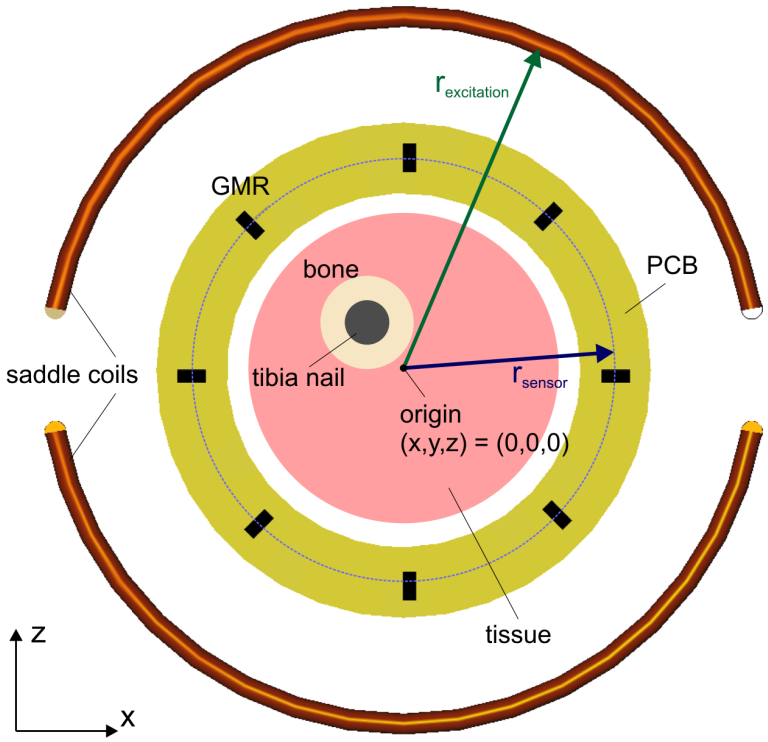

Fig. 1.9: Geometry of the excitation system, the sensor system and the tibia nail surrounded by low-conductive material (bone, tissue). The bone and the tibia nail are not centered due to the anatomy of the human leg.

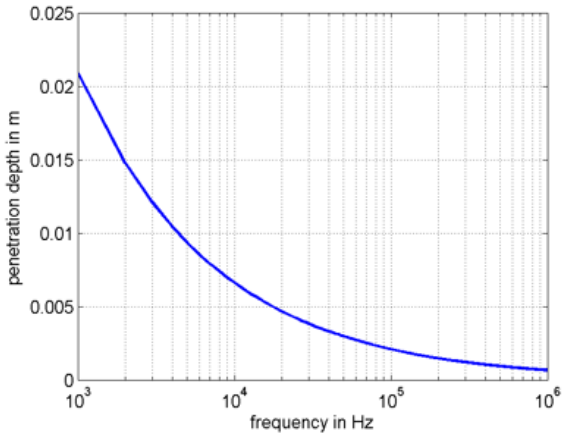

Fig. 1.10: Penetration depth at different frequencies with $\sigma = 58 \cdot 10^4 \frac{\mathrm{A}}{\mathrm{Vm}}$ for a tibia nail.

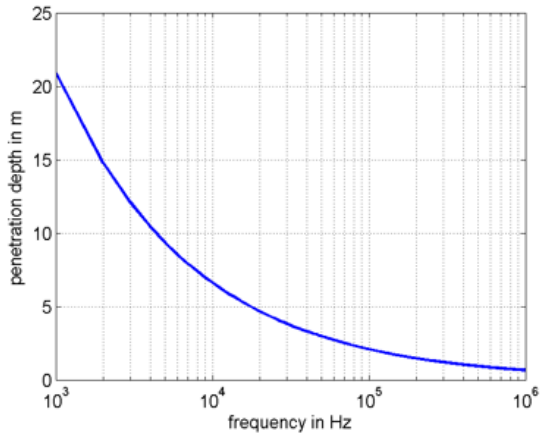

Fig. 1.11: Penetration depth at different frequencies with $\sigma = 0.5 \frac{\mathrm{A}}{\mathrm{Vm}}$ for surrounding material (human tissue).

1.6 Identification Strategy

Measurements have shown that the signal changes due to inhomogeneities in the tibia nail are very small and thus difficult to measure. Therefore, a ring with a higher conductivity was placed around the middle drill hole (1.12) to amplify the inhomogeneity and, furthermore, the signal. In fact, biomedical compatibility of the additional ring must be ensured for a medical application. However, in this work a copper ring with a ten times higher conductivity is assumed.

Before an inverse problem can be solved, the forward problem has to be formulated and a

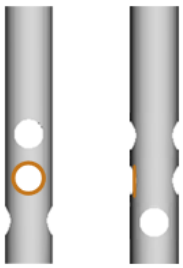

Fig. 1.12: Additionally used copper ring on the middle drill hole to amplify the eddy current effect.

corresponding simulation model has to be developed. Therefore, a finite element model was used in this work and thus the forward problem solutions are solved numerically. The copper ring was considered only in the simulation model, while the tibia nail was neglected. This simplification can be done since the significantly higher conductivity of the ring dominates the eddy current effect. Furthermore, the measurement system presented in Fig. 1.6 was extended by two GMR layers to realize improved spatial resolution. The configuration used in the simulation model is schematically shown in Fig. 1.13.

Solving real-life inverse problems is a special challenge since they are non-linear and ill-posed in common, [7]. Iterative optimization methods can be used to solve such inverse problems and regularization has to be applied to improve the convergence. Deterministic as well as stochastic methods are applicable, however, each method has its pros and cons. Deterministic

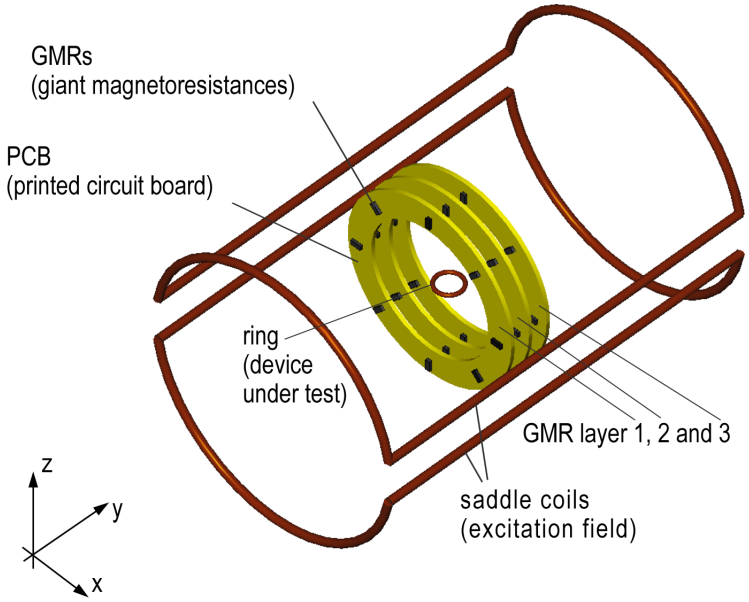

Fig. 1.13: Schematic measurement configuration with all relevant components for the simulation.

optimization techniques are fast and accurate while stochastic methods are able to find the global optimum. Large-scale inverse problems with a high number of parameters will not be solvable in an adequate time with stochastic optimization methods. However, the problem in hand has 5 parameters and therefore stochastic methods are reasonable, especially since it is a basic requirement to obtain the global solution. Nevertheless, computation time is important too and thus a combination of a deterministic and a stochastic method will also be investigated.

2 Forward Problem

Before an inverse problem can be solved, a numerical model of the underlying physics for the forward problem must be formulated. The input parameters of the forward problem at hand are the positioning parameters x_{obj}, y_{obj}, z_{obj} and the angle parameters ϑ_{obj} and φ_{obj} of the object (Fig. 2.1) while the outputs are the magnetic flux densities $\mathbf{B}$ measurable in the magnetic sensors, the GMR sensors. A copper ring is acting as the object in this case, but the forward problem formulation is valid for arbitrary shaped conductive objects.
A 3D finite element method (FEM) with an appropriate eddy current formulation based on Maxwell's equations was used to solve the present forward problem. The FEM as well as the formulation are described in detail in this section.

Since non-linear inverse problems need iterative algorithms to be solved, the forward problem has to be computed several times with different inputs. Therefore, an approximation of the forward solution is inevitable (model order reduction), provided that the accuracy stays sufficiently high. A model order reduction method was investigated and is described in Section 2.3.1.

2.1 Formulation

The $\mathbf{A}, V - \Phi$ formulation [8] was chosen to solve the eddy current problem with EleFAnT3D (Electromagnetic Field Analysis Tools) program package [9]. The formulation is based on the

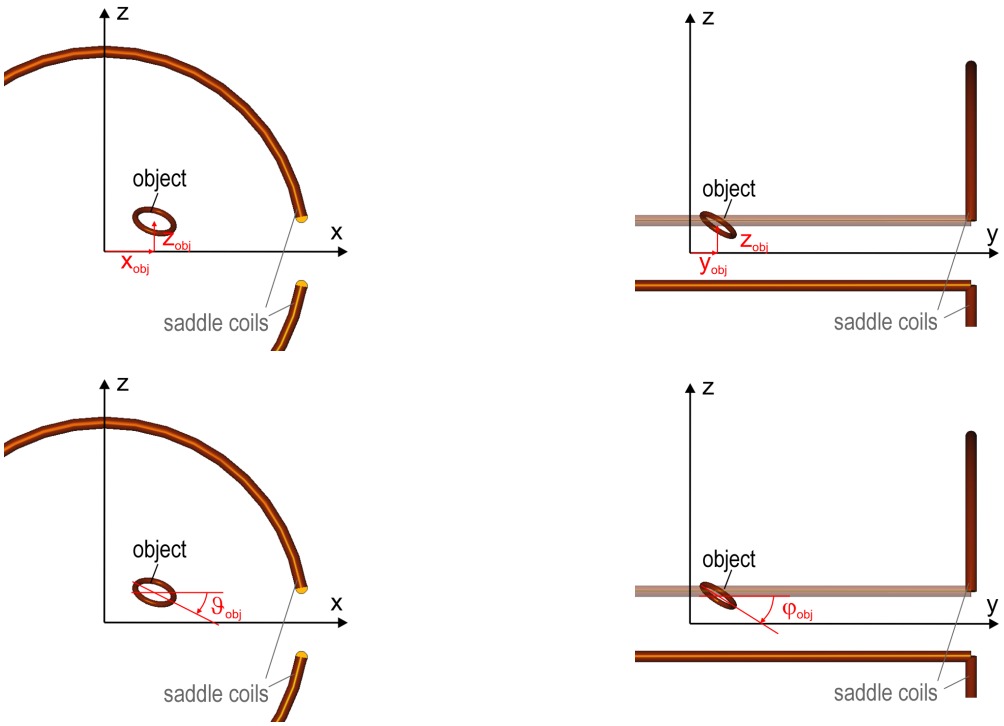

Fig. 2.1: Definition of the object parameters $(x, y, z, \vartheta, \varphi)_{obj}$.

Maxwell's Equations for electromagnetic fields,

$$\text{curl } \mathbf{H} = \mathbf{J} + \frac{\partial \mathbf{D}}{\partial t} \tag{2.1}$$

$$\text{curl } \mathbf{E} = -\frac{\partial \mathbf{B}}{\partial t} \tag{2.2}$$

$$\text{div } \mathbf{B} = 0 \tag{2.3}$$

$$\text{div } \mathbf{D} = \rho \tag{2.4}$$

where $\mathbf{H}$ is the magnetic field density, $\mathbf{J}$ is the current density, $\mathbf{E}$ is the electric field intensity, $\mathbf{B}$ is the magnetic flux density, $\mathbf{D}$ is the electric displacement and ρ is the electric charge density.

The term $\frac{\partial \mathbf{D}}{\partial t}$ in (2.1) can be neglected because of the fact that the conduction current density $\mathbf{J}$ is much more higher than the displacement current in the present problem.

The material equations are given by

$$\mathbf{J} = \sigma\, \mathbf{E}$$

$$\mathbf{B} = \mu\, \mathbf{H}$$

where σ is the electric conductivity and μ the permeability.

2.1.1 $\mathbf{A}, V - \Phi$ Formulation

The field components in the $\mathbf{A}, V - \Phi$ formulation are expressed with the magnetic vector potential $\mathbf{A}$ and the electric scalar potential V in the conducting region and the magnetic scalar potential Φ in air (non-conducting region).
The excitation is produced by a pair of geometrically opposed saddle coils with a given source current density $\mathbf{J}_s$. The resulting magnetic source field caused by the coils can be described by (2.5).

$$\text{curl}\, \mathbf{H}_s = \mathbf{J}_s \tag{2.5}$$

In the non-conducting region the magnetic field intensity $\mathbf{H}$ can be split into two parts, $\mathbf{H}_s$ and $\mathbf{H}_{ec}$. $\mathbf{H}_s$ is the source field part given in (2.5). $\mathbf{H}_{ec}$ is the part coming from either magnetized material or, as in this problem, from eddy currents flowing in the conductive region. $\mathbf{H}_{ec}$ is of course a curl-free field, (2.6), and can therefore be expressed as the gradient of a scalar magnetic potential Φ (2.7)

$$\text{curl}\, \mathbf{H}_{ec} = 0 \tag{2.6}$$

$$\mathbf{H}_{ec} = -\text{grad}\, \Phi \tag{2.7}$$

The total field $\mathbf{H}$ in this region is then:

$$\mathbf{H} = \mathbf{H}_s - \text{grad}\, \Phi. \tag{2.8}$$

There is no need to model the coils in the finite element mesh since the magnetic source field can be analytically calculated from the Biot-Savart's law.

For the eddy current region the magnetic vector potential $\mathbf{A}$ can be used to express the magnetic flux density $\mathbf{B}$

$$\mathbf{B} = \text{curl } \mathbf{A}. \tag{2.9}$$

by taking advantage of (2.3). Together with (2.2) this leads to the electric field intensity $\mathbf{E}$ in the conducting region:

$$\mathbf{E} = -j\omega\mathbf{A} - j\omega\text{grad } V. \tag{2.10}$$

With equations (2.5) - (2.10) all field components of the $\mathbf{A}, V - \Phi$ formulation are defined and can numerically be solved.

2.2 3D Finite Element Model

A 3D time harmonic eddy current finite element model is used to calculate the magnetic field components. Inside of the two saddle shaped coils, which are modelled as filamentary current sources, the conducting object is placed. For the sake of simplicity all investigations were done only with the copper ring since its 10 times higher conductivity dominates the eddy current effect of the hidden object. Nevertheless, the formulation holds for both, the nail/ring model and the model with the ring only.

The mesh consists of 17 408 finite brick elements and the solution, i. e. the magnetic flux density vector $\mathbf{B}$, is calculated using a $\mathbf{A}, V - \Phi$ formulation (2.1.1) in approximately 10 minutes using a PC with 3.16 GHz and 8 GB RAM. A detailed description of the FEM model can be found in [10]. The mesh is designed for a ring-shaped conducting object, which can be attached on the tibia nail mentioned in Section 1.5.

A sinusoidal filamentary current with an amplitude of 2 A_{ss} and a frequency of 100 kHz is impressed. The mesh is modularly implemented which means that its coordinates depend on the current object position and orientation. The geometry of the mesh, the eddy current distribution of the zoomed ring and field plots of all components of $\mathbf{B}$ as well as the absolute value in the region of interest are shown in Fig. 2.2, Fig. 2.3 and Fig. 2.7 - 2.10 respectively. These figures show the undisturbed field, i.e. no conductive object was assumed in order to give an impression about the field characteristic and the intensities of the source field in all directions.

The magnetic flux densities can be obtained directly as the curl of $\mathbf{A}$ in a post processing

step. Exemplary simulated values of the undisturbed field are shown in Fig. 2.11-2.13 for a measurement configuration given in Fig. 2.4. Different GMR orientations (x-, y- and z-direction, see Fig. 2.5) are considered to give a feeling of the characteristic and the magnitude for different configurations. Each diagram contains all three GMR layers, thus, the first and the last n values are from the outer layers and the middle n values are from the middle layer. n is the number of GMR sensors per layer and $n = 36$ in this case. Because of symmetry of the undisturbed field, the sensor positions were assumed to be located on one half of the ring only in this evaluation.

Since the GMR sensors are sensitive with respect to a certain direction - the axis of sensitivity - only, the cartesian components of the field values must be combined in all evaluations obtained by the numerical model to match the measurement values. For a radial layout of the GMR sensors (Fig. 2.4), the simulated field values are shown in Fig. 2.6. Details on calculating the flux density $\mathbf{B}$ in a certain direction can be found in the appendix, A.3. It has to be mentioned at this point that due to the measurement characteristic of an unipolar GMR only positive values can be measured (recall Fig. 1.4). Thus, information about the field direction gets lost.

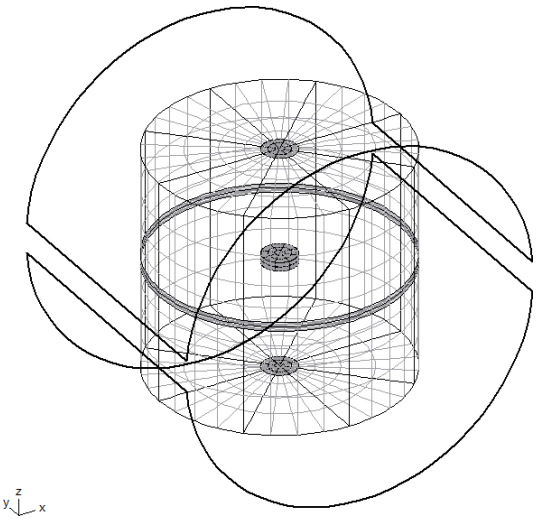

Fig. 2.2: Mesh of 3D FEM model with a copper ring representing the hidden conductive object.

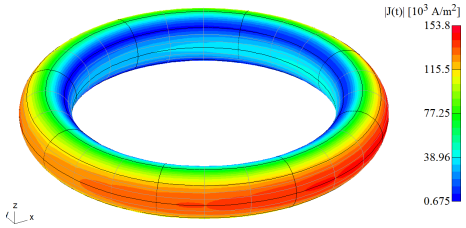

Fig. 2.3: Eddy current distribution in the ring located at the origin.

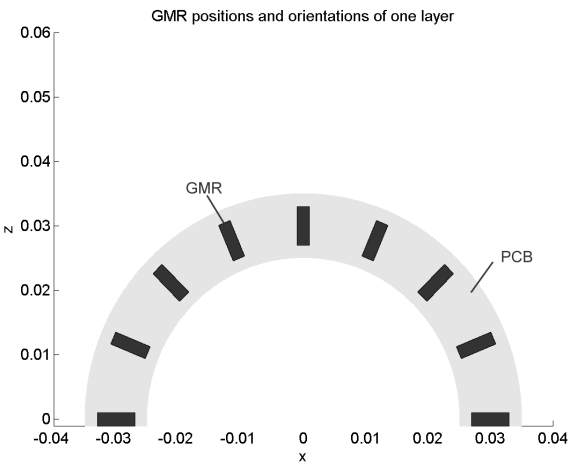

Fig. 2.4: Radial configuration of GMR sensors on a half ring-shaped printed circuit board.

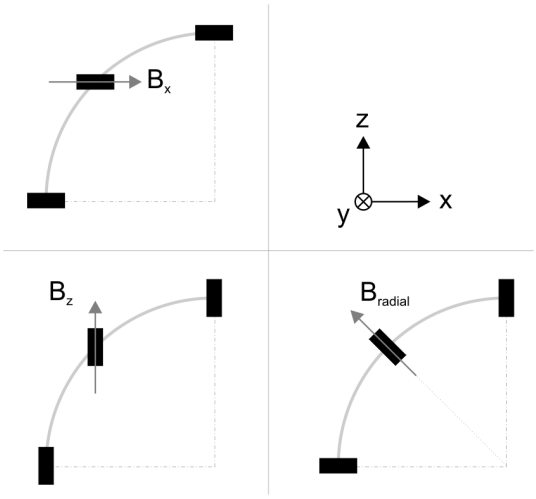

Fig. 2.5: Illustration of different GMR sensor orientations.

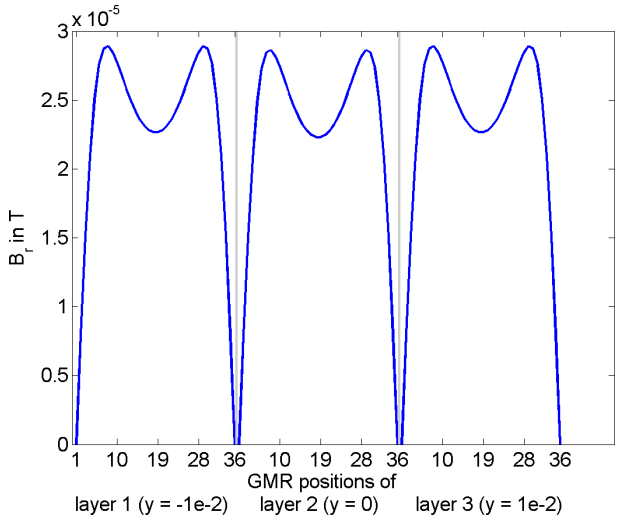

Fig. 2.6: Simulated field values in the case of radial oriented GMR sensors of the undisturbed field.

2.3 Model Order Reduction

Solving inverse problems always means solving the forward problem more than once. To reach reasonable computation times for the identification process, approximation methods for solving the forward problem are necessary. This can be done, for instance, by evaluating a number of parameter configurations prior to the identification process and by using these values

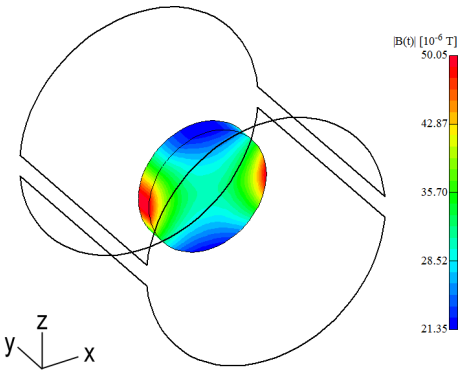

Fig. 2.7: Field plot of the absolute value of the magnetic flux density in the region of interest without a conductive object (undisturbed field).

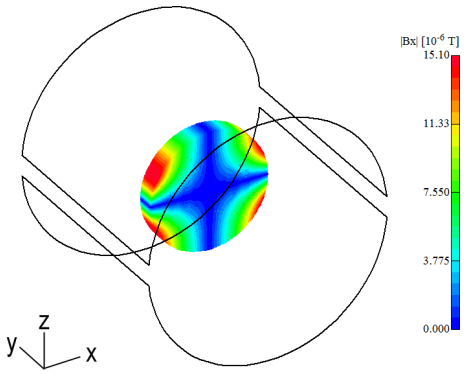

Fig. 2.8: Field plot of the x-component of the magnetic flux density in the region of interest without a conductive object (undisturbed field).

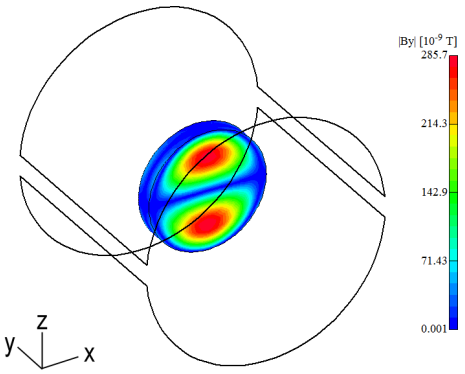

Fig. 2.9: Field plot of the y-component of the magnetic flux density in the region of interest without a conductive object (undisturbed field). The maximum value is much lower compared to the other components.

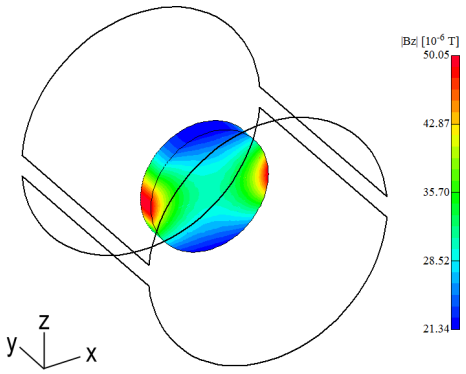

Fig. 2.10: Field plot of the z-component of the magnetic flux density in the region of interest without a conductive object (undisturbed field).

with some interpolation method during the identification process. Due to the requirement of a precise measurement system, the error of the chosen approximation method must be investigated before going on with procedures based on the approximated forward solution. Keeping the approximation error small is more difficult in non-linear problems than in linear problems. Since the problem region is bound, a sufficient number of pre-calculated solutions can be provided to meet the desired accuracy.

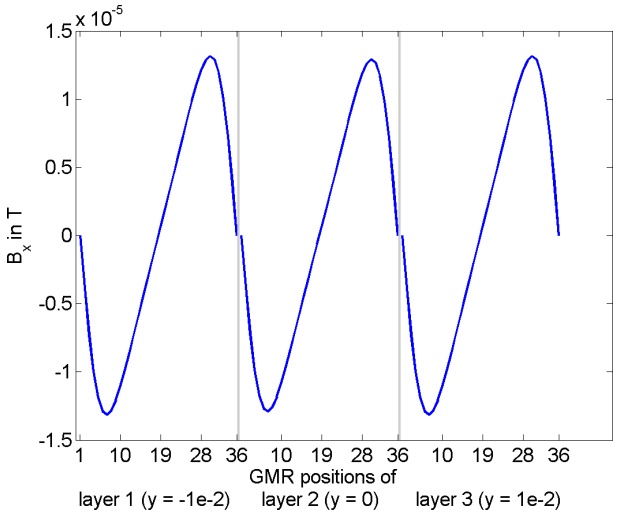

Fig. 2.11: Simulated field values with GMR orientations in x-direction of the undisturbed field.

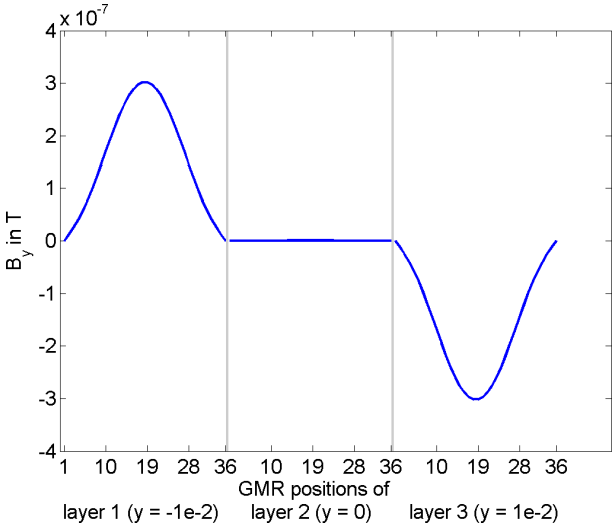

Fig. 2.12: Simulated field values with GMR orientations in y-direction of the undisturbed field.

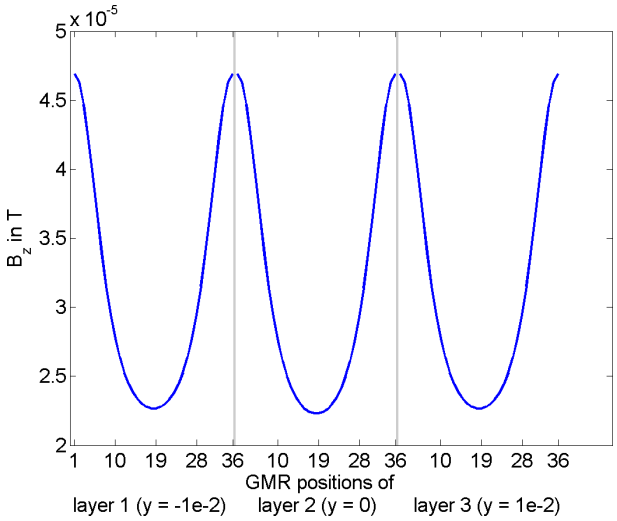

Fig. 2.13: Simulated field values with GMR orientations in z-direction of the undisturbed field.

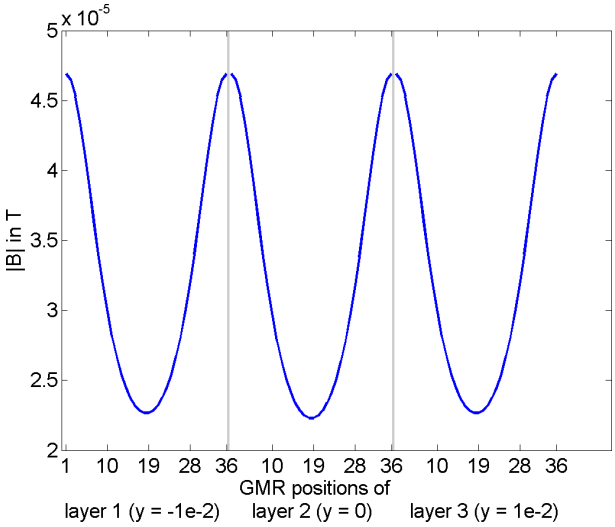

Fig. 2.14: Absolute values of the simulated field values vectors of the undisturbed field.

The approximation method selected for the forward problem at hand requires two phases. The first phase (training phase or FEM phase) is very time-consuming but is done only once prior to the actual identification process. The second phase is much faster which is crucial for solving the inverse problem.

2.3.1 Approximation with Precomputed Eddy Currents

This type of approximation is very specific to the present problem, especially to the shape of the object. But it provides a fast and simple method to become acquainted with the properties and the behavior of the model. The simplification starts by assuming a copper ring as hidden object instead of an arbitrary shaped object. The eddy currents flowing through the ring can be assumed as filament currents and hence the magnetic field can be calculated with the help of Biot-Savart's law, i.e. an analytic solution exists and no FEM solver is needed for this part of calculation. However, the eddy currents depend on the position and orientation of the copper ring in the excitation field. Therefore, they must be calculated numerically in an appropriate number of sampling positions (first phase). Since this information must be available before the identification algorithm starts, eddy currents are computed in a defined number of discrete values of the given parameters. Table 2.1 summarizes the selected positions.

Once the current in the ring is known for a sampling position, the magnetic flux den-

Table 2.1: Object parameter constraints and step sizes used for the FEM calculation to obtain the eddy currents at $9 \times 9 \times 9 \times 9 \times 5 \times 5 = 18\,225$ different object positions.

	x in mm	y in mm	z in mm	ϑ in °	φ in °
min	-20	-20	-20	-10	-10
max	20	20	20	10	10
step size	5	5	5	5	5

sity $\mathbf{B}$ of the current-carrying ring can be obtained by applying Biot-Savart's law (2.11) in a second phase.

$$\mathbf{B}(\mathbf{r}) = \frac{\mu}{4\pi} I(\mathbf{p}) \int \frac{d\mathbf{l}' \times (\mathbf{r} - \mathbf{r}')}{|\mathbf{r} - \mathbf{r}'|^3}. \tag{2.11}$$

$I(\mathbf{p})$ is the total current at the position $\mathbf{p} = (x, y, z, \vartheta, \varphi)_{obj}$, $\mathbf{r} - \mathbf{r}' = \hat{\mathbf{r}}$ denotes the displacement vector between the field point $\mathbf{r}$ and the source point $\mathbf{r}'$, $d\mathbf{l}$ is the differential element vector of the ring (Fig. 2.3.1) and μ is the permeability and set to μ_0 in this case.

Since the total currents are only available in the nodes of the discrete grid (calculated in the first phase), the current has to be interpolated for all positions in between. Fortunately, the characteristics of $I(\mathbf{p})$ is continuous in each parameter direction and therefore a cubic

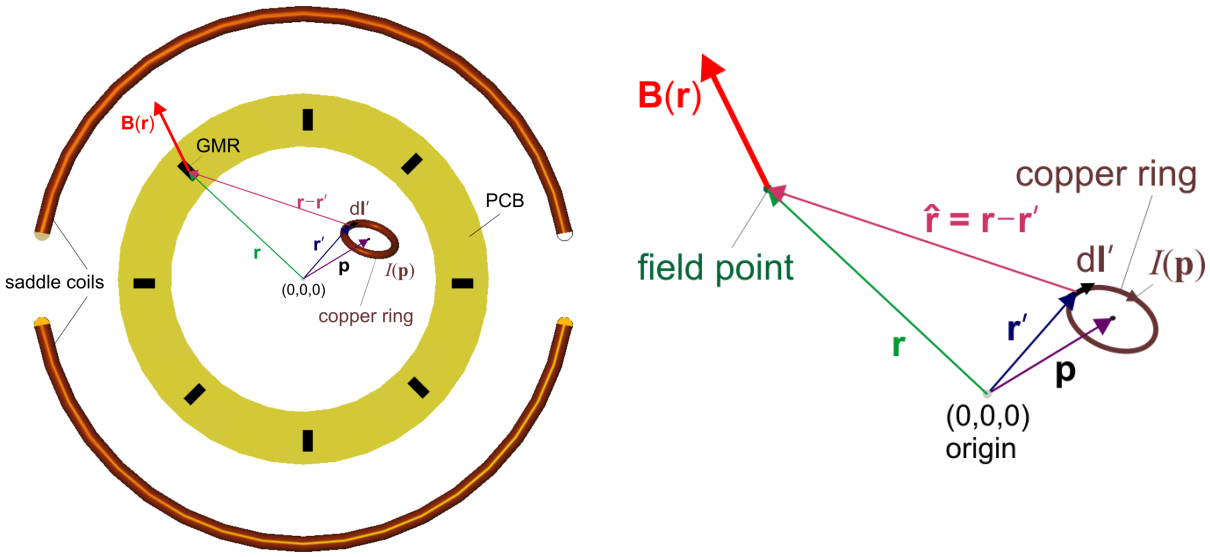

Fig. 2.15: Illustration of the geometric parts for calculating the magnetic flux density in point **r** assuming the ring position **p**.

interpolation with a very small loss of accuracy can be applied. In Fig. 2.16(a)-2.16(e) the calculated eddy currents in the nodes and the interpolation between them are shown for each parameter separately.

Assuming an arbitrary point $\mathbf{p}_t = (-7\,\text{mm}, 1.4\,\text{mm}, 8\,\text{mm}, 9°, -8°)$, the interpolation provides a total current of $I(\mathbf{p}_t)_{interpol} = 54.319\,\text{mA}$ while the exact solution is $I(\mathbf{p}_t)_{exact} = 54.364\,\text{mA}$ [1], which means a relative deviation of 0.08%. This is a very small value, but the effect of the eddy current deviation on the final simulation results has to be examined. Therefore, the two signals, calculated with the exact and the interpolated current respectively, are illustrated in Fig. 2.17. For the quantification of the approximation error due to the current interpolation, the ℓ-2-norm of the residuals were considered (2.12) and amounts to $1.2734 \cdot 10^{-10}\,\text{T}$ for the test point $\mathbf{p}_t$.

$$error_{approx} = \sqrt{\sum_{i=1}^{n_{GMR}} \left(B_{exact,i} - B_{interpol,i}\right)^2} \tag{2.12}$$

In summary it can be stated that the approximation error due to eddy current interpolation is negligible and all further investigations can be done using this approximation method. The computation time for the first phase, i.e. the FEM calculations (18 225 different object

[1] Exact means calculated with the described FEM code in this context.

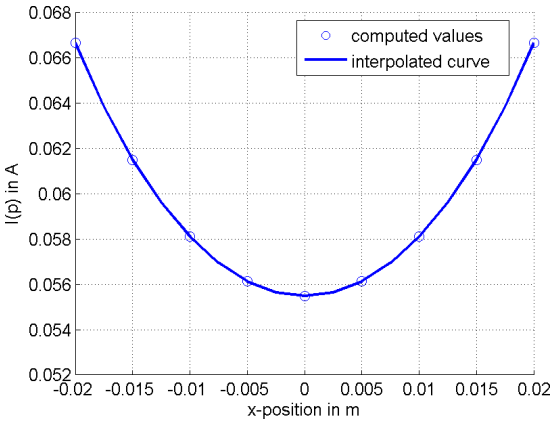

(a) $I = f(x), \quad (y, z, \vartheta, \varphi) = (0, 0, 0, 0)$

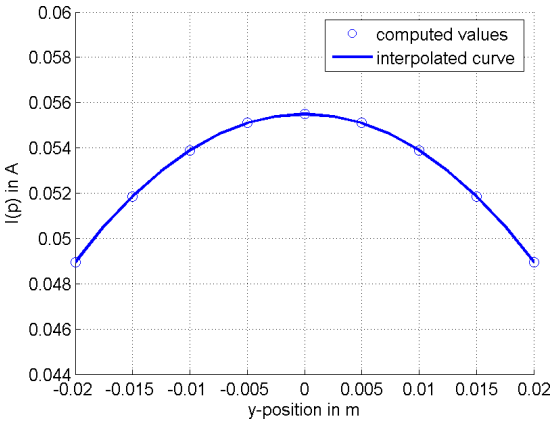

(b) $I = f(y), \quad (x, z, \vartheta, \varphi) = (0, 0, 0, 0)$

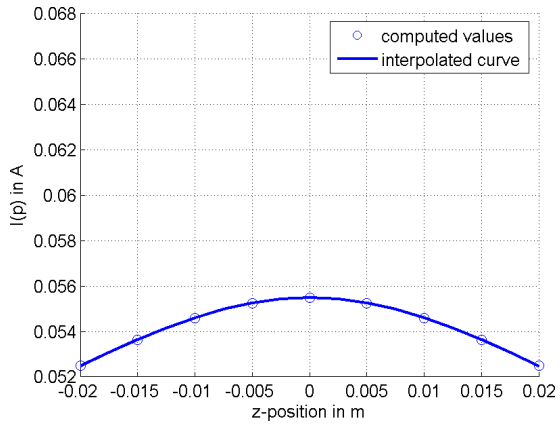

(c) $I = f(z), \quad (x, y, \vartheta, \varphi) = (0, 0, 0, 0)$

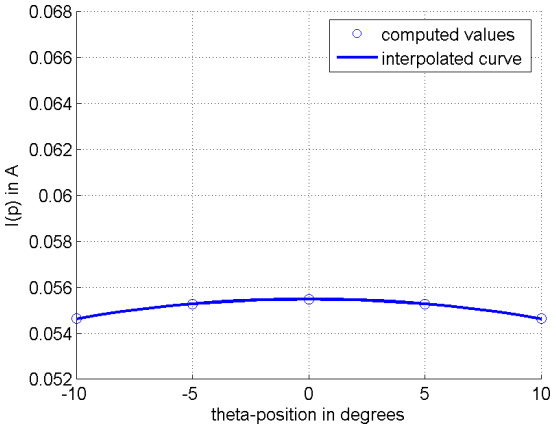

(d) $I = f(\vartheta), \quad (x, y, z, \varphi) = (0, 0, 0, 0)$

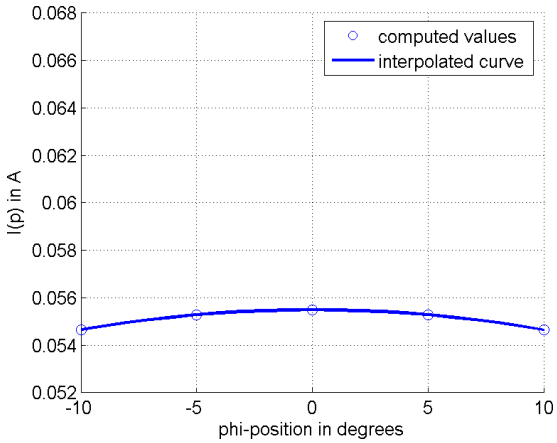

(e) $I = f(\varphi), \quad (x, y, z, \vartheta) = (0, 0, 0, 0)$

Fig. 2.16: Calculated and interpolated eddy currents $I(\mathbf{p})$ in the copper ring.

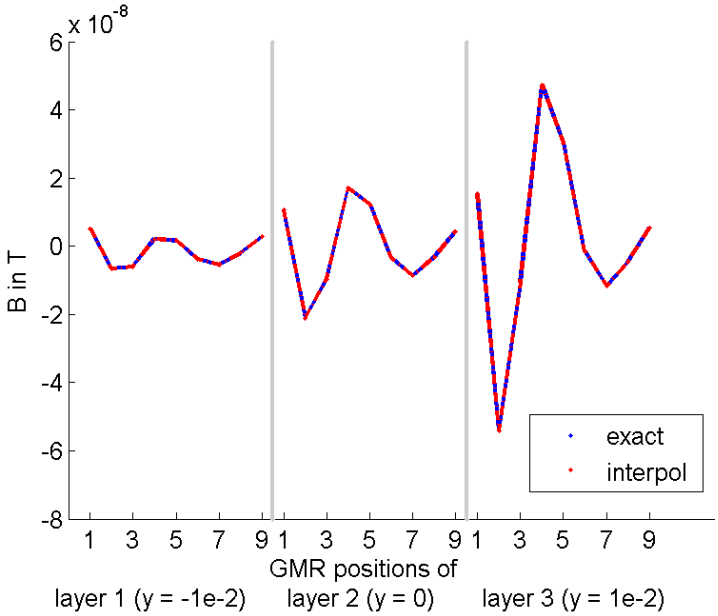

Fig. 2.17: Simulation results using the exact vs. the interpolated total current at the test point $\mathbf{p}_t$.

positions in the 5 dimensional parameter space times 600 seconds each) takes about 4 months. Each function call of the forward problem solver in the second phase (the identification process), takes 0.13 seconds for the interpolation and 0.11 seconds for numerically solving the integral of (2.11) or (A.1) respectively. This means that the goal of a significant decrease of the forward problem computation time at an acceptable accuracy is reached with this approximation method.

3 Sensitivity Analysis

The sensitivity of a set of measurements (B_i in $i = 1, \cdots, n$ observation points) depending on the variation of the parameters $\mathbf{p} = (x, y, z, \vartheta, \varphi)^\mathsf{T}$ is of major importance when solving the given inverse problem.
The individual sensitivities

$$\nabla \mathrm{B}_i = \begin{pmatrix} \frac{\partial B_i}{\partial x} \\ \frac{\partial B_i}{\partial y} \\ \frac{\partial B_i}{\partial z} \\ \frac{\partial B_i}{\partial \vartheta} \\ \frac{\partial B_i}{\partial \varphi} \end{pmatrix} \tag{3.1}$$

are influencing to a large extent the convergence speed and the convergence stability. The sensitivity of a measurement configuration can be mathematically defined by changes in the observed measurement data divided by the parameter changes causing them. The higher the sensitivity, the better the results of the inverse problem can be expected. Better means fast and accurate in this case.
The sensitivities can be summarized in the Jacobian matrix for a parameter state $\mathbf{p}$:

$$\mathrm{S}(\mathbf{p}) = \begin{bmatrix} \frac{\partial B_1}{\partial x} & \cdots & \frac{\partial B_n}{\partial x} \\ \frac{\partial B_1}{\partial y} & \cdots & \frac{\partial B_n}{\partial y} \\ \frac{\partial B_1}{\partial z} & \cdots & \frac{\partial B_n}{\partial z} \\ \frac{\partial B_1}{\partial \vartheta} & \cdots & \frac{\partial B_n}{\partial \vartheta} \\ \frac{\partial B_1}{\partial \varphi} & \cdots & \frac{\partial B_n}{\partial \varphi} \end{bmatrix} \tag{3.2}$$

$B_1 ... B_n$ are the observed magnetic flux density values in the sensitivity direction under investigation at the measurement points (GMR sensors), n is the number of GMR sensors and x, y, z, ϑ and φ are the object's parameters. Because of non-linearity of the given

problem, the Jacobian matrix (or sensitivity matrix) must be evaluated in each position and orientation of the ring ($\mathbf{p} = (x, y, z, \vartheta, \varphi)$) separately. Nevertheless, a way to quantify the sensitivities of the measurement system with respect to each parameter separately, has to be found, since knowledge about it is necessary for the subsequent identification process.

First of all, the parameter state $\mathbf{p}_0 = (0, 0, 0, 0, 0)$ was chosen to get an idea about the characteristics of the sensitivity matrix. One element $S_{i,j}$ of the sensitivity matrix can be calculated by computing numerically the center gradient for a sensor j and a parameter i:

$$S_{i,j} = \frac{B_j(x_i + \Delta x_i) - B_j(x_i - \Delta x_i)}{2\Delta x_i}. \tag{3.3}$$

The sensitivities of all measurement sensors with respect to parameter changes based on the ring position $\mathbf{p}_0$ are summarized in Fig. 3.1, where the sensitivities are expressed by the samples of the box plot. The 3x8 (PCB layers x sensors per layer) sensors are radially configured (see Fig. 2.4) along a ring. It becomes obvious that the angle parameters have

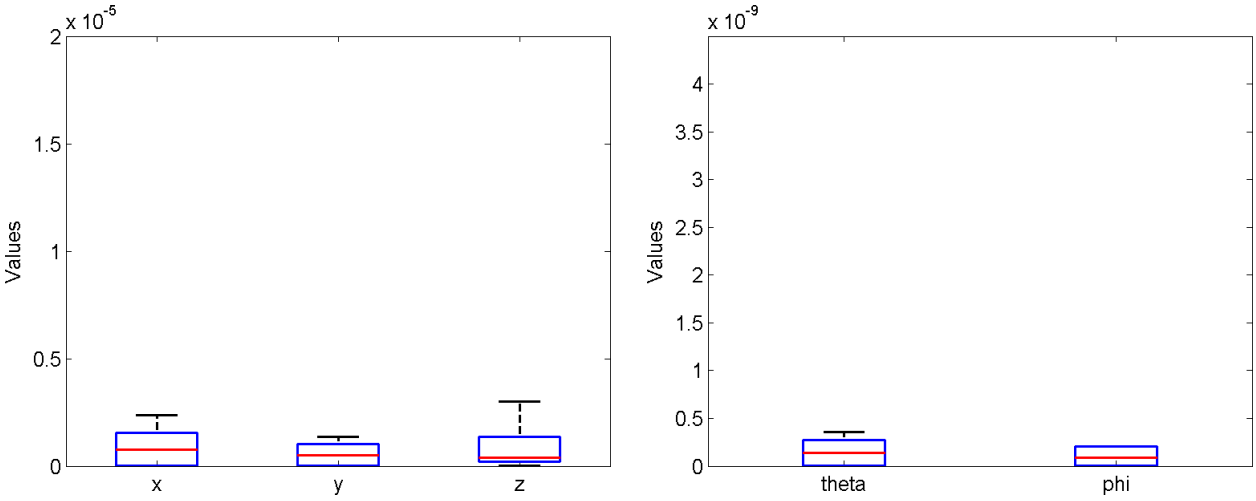

Fig. 3.1: Box plot of all sensitivity values for one single object position grouped by parameters. The plot was divided in positioning and angle parameters due to very different sensitivity value ranges. Red line: mean value of all samples; blue lines: lower and upper quartile; black lines: minimum and maximum values.

a very low sensitivity compared to the positioning parameters (about 4 decades, $\frac{10^{-5}}{10^{-9}}$) in the current configuration. This fact could change at other ring positions or using other GMR configurations. Hence, a second position $\mathbf{p}_1 = (-1\,\text{cm}, -1\,\text{cm}, -1\,\text{cm}, -5\,^\circ, -5\,^\circ)$ was

evaluated with the same GMR configuration and the result is shown in Fig. 3.2. Again, the difference between positioning and angle parameters is extremely high. On the other hand, this second ring position shows higher maximum sensitivities but smaller mean sensitivities than the first one.

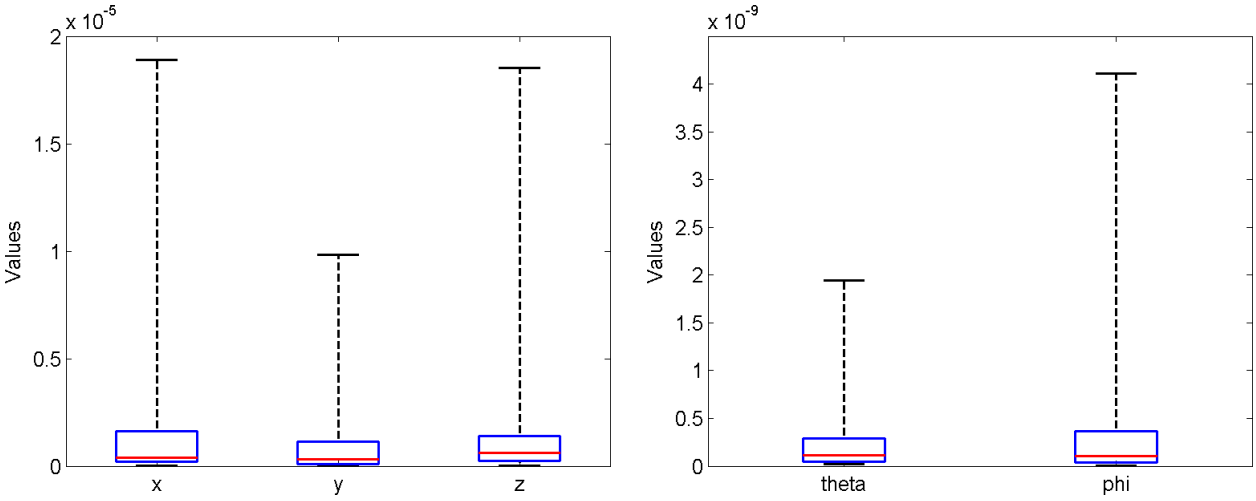

Fig. 3.2: Box plot of all sensitivity values for one single object position $\mathbf{p}_1$ grouped by the parameters.

To investigate whether other sensor configurations may increase the overall sensitivity, a set of equally distributed parameter states throughout the whole parameter space were chosen and the sensitivities were calculated. Besides the already described radial configuration, two other possibilities of GMR orientations were chosen, namely in x- and in z-direction (see Fig. 3.3). Mean and maximum sensitivity values of the three configurations are shown in Table 3.1.

The setup in z-direction shows a very low sensitivity and does not deserve further investigation. Placing the GMR sensors in x-direction or in radial direction seems to be much more promising as Table 3.1 shows. Since the mean value is responsible for a stable convergence of the inverse algorithm, the radial configuration was chosen.

It has been shown that the sensitivities strongly depend on the parameter values. Furthermore, the sensitivities of the angle parameters (ϑ, φ) are definitely lower than the ones of the positioning parameters (x,y,z), independent from the parameter state. It has to be expected that the identification of the angle parameters will be a challenging task.

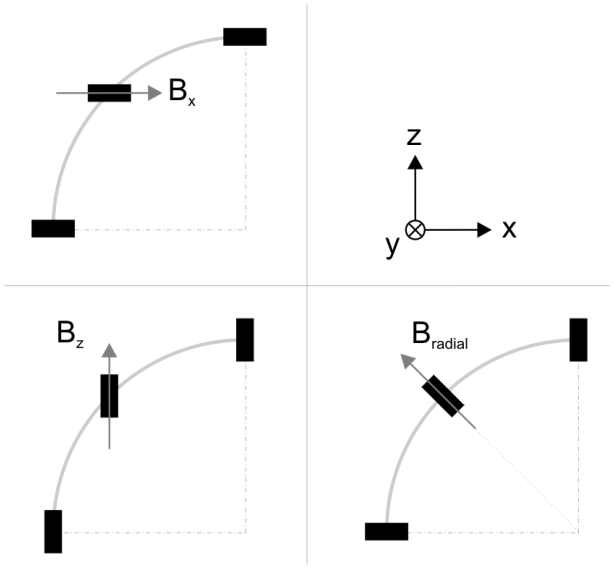

Fig. 3.3: Different GMR sensor orientations assumed for sensitivity investigations.

Table 3.1: Parameter sensitivities assuming three different measurement configurations. The bold entries are the winners of the corresponding sensitivity category.

	min. sensitivity				
	x	y	z	ϑ	φ
x-config	**1.4E-09**	3.6E-10	1.8E-10	**2.2E-14**	**2.5E-14**
z-config	7.9E-10	4.4E-11	2.3E-10	1.5E-15	2.2E-14
r-config	3.9E-11	**1.1E-09**	**5.2E-10**	1.5E-15	**2.5E-14**
	max. sensitivity				
	x	y	z	ϑ	φ
x-config	3.3E-4	1.7E-4	**2.7E-4**	**1.4E-7**	**1.0E-7**
z-config	2.6E-4	1.3E-4	2.6E-4	1.1E-7	7.6E-8
r-config	**3.9E-4**	**1.8E-4**	2.2E-4	**1.4E-7**	9.4E-8
	mean sensitivity				
	x	y	z	ϑ	φ
x-config	2.6E-6	2.1E-6	2.6E-6	1.0E-9	7.8E-10
z-config	2.6E-6	1.9E-6	2.8E-6	1.0E-9	6.8E-10
r-config	**2.8E-6**	**2.6E-6**	**2.9E-6**	1.0E-9	**8.6E-10**

4 Inverse Problem

Inverse problems seek to find the unknown cause for observed or measured effects in physical systems. The task of solving inverse problems arises in many fields of science, as for instance in geophysics, computer vision, medical imaging and non destructive testing. Typically, inverse problems are ill posed, i.e. a simple inversion of the forward problem is unrewarding. Thus, appropriate measures, known as regularization, have to be taken to stabilize the inversion methods.
In this chapter the theory of inverse problems and challenges arising with them are depicted. Furthermore, deterministic as well as stochastic concepts for solving inverse problems are suggested and described in detail. The application of them to the present problem is the topic of the next chapter.

4.1 Inverse Theory

To illustrate the problems of inversion, a linear equation system with the unknown parameter vector $\mathbf{x}$, the measurement data vector $\mathbf{y}$ and the system matrix A can be assumed:

$$\mathbf{y} = \mathrm{A}\mathbf{x} \tag{4.1}$$

(4.1) can be solved by simply inverting the system matrix.

$$\mathbf{x} = \mathrm{A}^{-1}\mathbf{y} \tag{4.2}$$

The first constraint is that A must be quadratic to be inverted. Although this is the case, the condition of the linear equation system must be considered. The following example will

show how the condition number will affect the inversion result.

Example:

Consider the 2 x 2 system

$$\begin{bmatrix} 1 & 1 \\ 1 & 0.999 \end{bmatrix} \begin{Bmatrix} x_1 \\ x_2 \end{Bmatrix} = \begin{Bmatrix} 0 \\ 1 \end{Bmatrix} \tag{4.3}$$

The solution is obtained as: $x_1 = 10^3,\ x_2 = -10^3$. Due to small errors in computation, the system changes to:

$$\begin{bmatrix} 1 & 1 \\ 1 & 1.001 \end{bmatrix} \begin{Bmatrix} x_1 \\ x_2 \end{Bmatrix} = \begin{Bmatrix} 0 \\ 1 \end{Bmatrix} \tag{4.4}$$

The solution of this second linear equation with only a very small difference in the system matrix compared to the first one, changes to $x_1 = -10^3,\ x_2 = 10^3$.
In this illustrative example, a small error in calculation of an element of the system matrix (error = 0.2%) caused an error of 200% in the solution. This is called an ill-conditioned system.
To quantify the condition of a matrix, the quotient κ of the largest (λ_n) and the smallest (λ_1) eigenvalue of the system matrix can be build:

$$\kappa = \frac{|\lambda_n|}{|\lambda_1|} = \frac{|1.9995|}{|-0.0005|} = 3\,998 \tag{4.5}$$

The higher the condition number, the more ill-conditioned is the system. If the measurements are not strongly linearly independent, the condition number is high and small input errors will cause big output errors. Unfortunately, this is the case in most of the practical applications. Thus, taking noise into account the calculated result will be completely distorted. Such a problem is termed "ill-posed". An inverse problem is well-posed if

- for all admissible data, the solution exists (existence),
- for all admissible data, the solution is unique (uniqueness) and
- the solution depends continuously on the data (stability).

Otherwise the inverse problem is ill-posed. These three conditions were defined by Hadamard, [7]. If the data are contaminated with noise, the third condition is not fulfilled and therefore the corresponding inverse problem is ill-posed. Alternative ways to find the parameters from observed data must be used.
Real life problems are also always non-linear, therefore the system matrix depends on the parameter and the forward problem changes to

$$\mathbf{y} = \mathrm{F}(\mathbf{x}) \tag{4.6}$$

with the forward problem operator $\mathrm{F}(\mathbf{x})$.
Taking data noise into account, (4.6) changes to

$$\mathbf{y}^{\delta} = \mathrm{F}(\mathbf{x}) \tag{4.7}$$

Here, δ is called the noise level.
Thus, the unknown parameter vector $\mathbf{x}$ must be identified to fulfill (4.7). Reword, the functional Ψ, i.e. the squared difference between the noisy measured data vector $\mathbf{y}^{\delta}$ and the forward problem solution $\mathrm{F}(\mathbf{x})$ calculated with an parameter vector $\mathbf{x}$, must be minimized:

$$\min_{x \in \mathbb{R}^n} \Psi = \left\| \mathrm{F(x)} - \mathbf{y}^{\delta} \right\|_2^2 \tag{4.8}$$

with $\|\cdot\|_2^2$ denoting the squared L2 norm of a vector, e.g.

$$\|\mathbf{x}\|_2^2 = \sum_{i=1}^{m} x_i^2$$

4.2 Concepts of Solving Inverse Problems

A number of optimization methods are available to solve the minimization problem (4.8), deterministic ones (e.g. Gauss-Newton method) as well as stochastic methods like Evolution Strategies, Genetic Algorithms, Simulated Annealing or Particle Swarm Optimization. While deterministic algorithms are commonly faster, stochastic algorithms work more globally.

4.2.1 Deterministic Methods

If more equations, i.e. observed data values, than unknown parameters exist, the system is overdetermined and the method of least squares can be used to minimize the functional (4.8). The most prominent algorithm to solve non-linear least square problems is the Gauss-Newton method. This method is adapted to minimize a sum of squared function values only. Its main advantage is that the Hessian matrix (which is composed from second order derivations) can be very nicely approximated by the Jacobian matrix (first order derivatives only).

4.2.1.1 Basic Gauss-Newton Algorithm

In Newton's method a quadratic model of the objective function is used in each iteration step k:

$$f(\mathbf{x}_k + \mathbf{p}) \approx f(\mathbf{x}_k) + \mathbf{g_k}(\mathbf{x})^\mathsf{T}\mathbf{p} + \frac{1}{2}\mathbf{p}^\mathsf{T}\mathrm{G}_k(\mathbf{x})\mathbf{p}. \tag{4.9}$$

$\mathbf{p}$ is the step to the minimum, $\mathbf{g}(\mathbf{x})$ is the gradient and $\mathrm{G}(\mathbf{x})$ is the Hessian matrix, i.e. the second derivative of $f(\mathbf{x})$. $\mathbf{p}_k$ becomes a stationary point if the linear equation system (4.10) is satisfied:

$$\mathrm{G}_k(\mathbf{x})\mathbf{p}_k = -\mathbf{g}_k(\mathbf{x}) \tag{4.10}$$

The solution $\mathbf{p}_k$ of (4.10) is called Newton direction.
In case of minimizing a least squares problem, the functional in (4.8) can be written as the sum of squares of the residuals r between the noisy measured data y^δ and the forward problem solution $F(\mathbf{x})$:

$$\begin{aligned} &r_i(\mathbf{x}) = F_i(\mathbf{x}) - y_i^\delta \qquad i = 1, 2, ..., m \\ &\mathbf{r} = (r_1, r_2, ..., r_m)^\mathsf{T} \\ &\min_{x \in \mathbb{R}^n} \Psi(\mathbf{x}) = \sum_{i=1}^{m} r_i(\mathbf{x})^2 = \mathbf{r}(\mathbf{x})^\mathsf{T}\mathbf{r}(\mathbf{x}) \end{aligned} \tag{4.11}$$

with m being the number of equations or measurements and n is the number of parameters. The $m \times n$ Jacobian matrix J of the residuals with respect to $\mathbf{x}$ can be written as

$$\begin{aligned} \mathrm{J}(\mathbf{x}) &= \begin{bmatrix} \frac{\partial r_1}{\partial x_1} & \cdots & \frac{\partial r_1}{\partial x_n} \\ \vdots & \ddots & \vdots \\ \frac{\partial r_m}{\partial x_1} & \cdots & \frac{\partial r_m}{\partial x_n} \end{bmatrix} \\ &= [\nabla r_1, \nabla r_2, \ldots, \nabla r_m]^\mathsf{T} \end{aligned} \tag{4.12}$$

and the gradient $\mathbf{g}(\mathbf{x})$ and the Hessian matrix $\mathrm{G}(\mathbf{x})$ of $\Psi(\mathbf{x})$ can now be exactly expressed using (4.12), [11]:

$$\mathbf{g}(\mathbf{x}) = 2\mathrm{J}(\mathbf{x})^\mathsf{T}\mathbf{r}(\mathbf{x}) \tag{4.13}$$

$$\mathrm{G}(\mathbf{x}) = 2\mathrm{J}(\mathbf{x})^\mathsf{T}\mathrm{J}(\mathbf{x}) + 2\sum_{i=1}^{m} r_i(\mathbf{x})\nabla^2 r_i(\mathbf{x}). \tag{4.14}$$

Ignoring the second term in (4.14), the Hessian matrix is approximated by

$$\mathrm{G}(\mathbf{x}) \approx 2\mathrm{J}(\mathbf{x})^\mathsf{T}\mathrm{J}(\mathbf{x}). \tag{4.15}$$

A method making use of (4.15) is called Gauss-Newton method.
Again, the Newton direction given in (4.10) can be written but, with the gradient and Hessian matrix defined for the Gauss-Newton method:

$$\mathrm{J}(\mathbf{x})^\mathsf{T}\mathrm{J}(\mathbf{x})\mathbf{p}_k = -\mathrm{J}(\mathbf{x})^\mathsf{T}\mathbf{r}(\mathbf{x}). \tag{4.16}$$

Thus, starting with an initial parameter vector $\mathbf{x}_0$, the algorithm finds a parameter update in each iteration k

$$\mathbf{x}_{k+1} = \mathbf{x}_k + \mathbf{p}_k \tag{4.17}$$

by solving the linear normal equation (4.16).
Due to non-linearity of the model, in each iteration step linearization is performed around the current parameter vector $\mathbf{x}_k$. The number of iterations needed to reach a certain minimum value strongly depends on the starting value $\mathbf{x}_0$.

4.2.1.2 Levenberg-Marquardt Method

The Hessian matrix can become indefinite in the Gauss-Newton method and, as a consequence, the algorithm fails to converge or converges slowly. Therefore a multiple of the identity matrix can be added to the Hessian matrix:

$$\left(\mathrm{J}(\mathbf{x})^{\mathsf{T}}\mathrm{J}(\mathbf{x}) + \nu\,\mathrm{I}\right)\mathbf{p}_k = -\mathrm{J}(\mathbf{x})^{\mathsf{T}}\mathbf{r}(\mathbf{x}) \qquad \nu \geq 0. \tag{4.18}$$

ν is selected in such a way that $\left(\mathrm{J}(\mathbf{x})^{\mathsf{T}}\mathrm{J}(\mathbf{x}) + \nu\,\mathrm{I}\right)$ becomes positive definite. Solving (4.18) iteratively with respect to the parameter update $\mathbf{p}_k$ is the method of Levenberg-Marquardt, [12], [13].
If $\nu \to 0$, the Levenberg-Marquardt algorithm is reduced to the Gauss-Newton method, if $\nu \gg$, $\mathbf{p}_k$ has the same direction as $-\mathbf{g}$. Starting with a large value of ν stabilizes the algorithm even if the initial guess of $\mathbf{x}$ is far away from the true solution.

4.2.1.3 Regularization

The Levenberg-Marquardt method can be used in principle to find the minimum of a non-linear minimization problem. Nevertheless, if the problem is ill-posed, i.e. $\mathrm{F}(\mathbf{x})$ fails to be continuously invertible or one has to deal with noisy data, regularization has to be applied. The most common method is known with the Tikhonov regularization that enables a stable approximated solution to be obtained for ill-posed problems. The idea of Tikhonov regularization is to convert the ill-posed problem in a well-posed one by adding some a-priori information to the minimization term:

$$\Psi = \left\|\mathrm{F}(\mathbf{x}) - \mathbf{y}^{\delta}\right\|_2^2 + \alpha\,\|\mathrm{L}\,(\mathbf{x} - \mathbf{x_0})\|_2^2 \tag{4.19}$$

L denotes some regularization matrix, α is the regularization parameter and $\mathbf{x_0}$ is some initial guess of $\mathbf{x}_{true}$. This additional regularization term is called penalty term since it penalizes solutions that are far away from the initial guess.

The gradient and the Hessian matrix are given by (4.20) and (4.21) with $\tilde{\mathbf{x}} = \mathbf{x} - \mathbf{x_0}$.

$$\begin{aligned}\frac{\partial}{\partial \tilde{\mathbf{x}}} \left(\alpha \left\|\mathrm{L}\tilde{\mathbf{x}}\right\|_2^2\right) &= \frac{\partial}{\partial \tilde{\mathbf{x}}} \left(\alpha \left((\mathrm{L}\tilde{\mathbf{x}})^{\mathsf{T}} (\mathrm{L}\tilde{\mathbf{x}})\right)\right) \\ &= \frac{\partial}{\partial \tilde{\mathbf{x}}} \left(\alpha \left(\langle \mathrm{L}\tilde{\mathbf{x}}, \mathrm{L}\tilde{\mathbf{x}} \rangle\right)\right) \\ &= \alpha \left(\langle \mathrm{L}, \mathrm{L}\tilde{\mathbf{x}} \rangle + \langle \mathrm{L}\tilde{\mathbf{x}}, \mathrm{L} \rangle\right) \\ &= 2\,\alpha \mathrm{L}^{\mathsf{T}} \mathrm{L}\tilde{\mathbf{x}} \end{aligned} \tag{4.20}$$

$$\frac{\partial^2}{\partial \tilde{\mathbf{x}}^2} \left(\alpha \left\|\mathrm{L}\tilde{\mathbf{x}}\right\|_2^2\right) = \frac{\partial}{\partial \tilde{\mathbf{x}}} \left(2\,\alpha \mathrm{L}^{\mathsf{T}} \mathrm{L}\tilde{\mathbf{x}}\right) = 2\,\alpha \mathrm{L}^{\mathsf{T}} \mathrm{L} \tag{4.21}$$

Typically the regularization matrix L is either the identity matrix, a discrete approximation to the first or second derivative operator or some approximation to the a-priori covariance matrix. α is a monotonically decreasing sequence of positive numbers whose starting value and decrease scheme must be found to provide a stable and fast inversion algorithm. Concepts of finding an adequate regularization sequence are, for instance, the discrepancy principle criterion [14] and the L-curve criterion. Since the discrepancy principle criterion and the L-curve criterion are working for linear systems only, the determination of the regularization parameter α must be a done in each iteration, i.e. in each linearization step, separately. This means that the forward problem must be solved several times to obtain the optimal α-value first in each iteration, before the actual approximation of the inverse problem solution can be performed. The consequence would be, a significant increase in computation time. Therefore, the method of trial and error is the better choice in the non-linear case.

4.2.1.3.1 The Method of Trial and Error A common way to find an appropriate sequence of α is to try and observe the behavior of the inverse problem solving algorithm. If the parameters converge very slowly, the regularization parameter must be decreased. If the algorithm gets instable, i.e. the parameters start to oscillate, α and therefore the regularization term must be increased. This process has to be repeated for different parameter states and initial values due to identify an appropriate sequence for a widely use inside the parameter ranges.

4.2.1.4 Iteratively Regularized Gauss-Newton Algorithm (IRGN)

Using Tikhonov regularization with the basic Gauss-Newton method, (4.16) is extended by the gradient (4.20) and the Hessian matrix (4.21) of the penalty term:

$$\left(\mathrm{J}(\mathbf{x})^{\mathsf{T}}\mathrm{J}(\mathbf{x}) + \alpha \mathrm{L}^{\mathsf{T}}\mathrm{L}\right)\mathbf{p}_k = -\mathrm{J}(\mathbf{x})^{\mathsf{T}}\mathbf{r}(\mathbf{x}) + \alpha \mathrm{L}^{\mathsf{T}}\mathrm{L}\,(\mathbf{x} - \mathbf{x}_0) \tag{4.22}$$

$\mathrm{J}(\mathbf{x})$ denotes the derivative of the forward operator, L is the regularization matrix, $\mathbf{x}_0$ is the initial guess or any assumed starting value, otherwise, and α is the regularization parameter. The iteratively regularized Gauss-Newton method was proposed by Bakushinskii [15] in 1992 and is widely used for reconstruction problems.

Pseudo code of the IRGN:

1. Initialization: Choose the regularization matrix L, $\mathbf{x}_0$ and α_0. Set $k = 0$.
2. Compute $\mathrm{F}(\mathbf{x}_k)$ and the residual $\mathbf{r}_k = (\mathrm{F}(\mathbf{x}_k) - \mathbf{y}^{\delta})$.
3. Compute the Jacobian matrix J at $\mathbf{x}_k$
4. Solve the equation $(\mathrm{J}(\mathbf{x}_k)^{\mathsf{T}}\mathrm{J}(\mathbf{x}_k) + \alpha_k \mathrm{L}^{\mathsf{T}}\mathrm{L})\,\mathbf{p}_k = -\mathrm{J}(\mathbf{x}_k)^{\mathsf{T}}\mathbf{r} + \alpha \mathrm{L}^{\mathsf{T}}\mathrm{L}(\mathbf{x}_k - \mathbf{x}_0)$ for $\mathbf{p}_k$ using a Preconditioned Conjugate Gradient (PCG) method or another numerical algorithm to solve large systems of linear equations.
5. Update the new parameter state $\mathbf{x}_{k+1} = \mathbf{x}_k + \mathbf{p}_k$.
6. Adapt α and set $k = k + 1$.
7. Repeat 2-6 until a sufficient stopping criterion is reached.

The way of choosing the initial values and the stopping criterion is shown in the chapter of results, 5.

4.2.2 Stochastic Methods

While in deterministic methods the computation is completely determined by the values sampled so far, stochastic methods use a random process and statistical information of the solutions already computed for computing the next parameter set. If there is no or very little knowledge about the behavior of the optimization problem, it is recommendable to start with stochastic strategies. Stochastic methods are mostly easy to implement and there is no need to compute higher order terms of the forward operator. Furthermore, stochastic algorithms are able to find the global optimum of the objective function and work more robust, which is important when data noise must be considered.
Among important and widely used stochastic optimization algorithms Simulated Annealing (SA), Swarm Optimization (SO), Genetic Algorithms (GA) and Evolution Strategies (ES) can be found. In this work the focus lies on Evolution Strategies, that are inspired by the behavior of biologic evolution.

4.2.2.1 Introduction to Evolution Strategies

In the mid 1960s Ingo Rechenberg, [16], [17], [18], and Hans-Paul Schwefel, [19], [20], from the Technical University of Berlin, Germany, started developing optimization methods inspired by nature taking Darwin's evolution principles into account. Recombination, mutation, competition and selection of individuals in a population are copied from biologic behavior and represent the core features of evolution strategies.
An individual in nature analogically means a set of optimization parameters and a set of individuals builds a generation. A generation itself is similar to one iteration in the evolution strategy. Since the number of ways to the best solution is infinite using stochastic algorithms, it is necessary to run more than one complete iteration process (each iteration is starting with a different initial generation) to check the reproducibility of the result. Therefore it is important to consider the computation time for solving the forward problem, since it is the most time consuming step of an evolution strategy. Thus, an important measure is the number of function calls needed to solve an optimization problem to a sufficient accuracy.
First, the core parts of evolution strategies are described in this section. Furthermore, a

higher order evolution strategy, which takes population into account, is depicted.

Recombination is the first part of creating genetic variability inside a population, where parent individuals are taken and combined to produce new descendants. The selection of the parents can be done in a completely random way or by taking the fitness of parents into account, i.e., the better a parent meets the objective, the higher is the probability to produce descendants. This method is called roulette-wheel selection or fitness proportional selection (Fig. 4.1). The probability p_i of each parent can be calculated with (4.23), where f is objective function value of a parent and N is the number of all parents in the current generation.

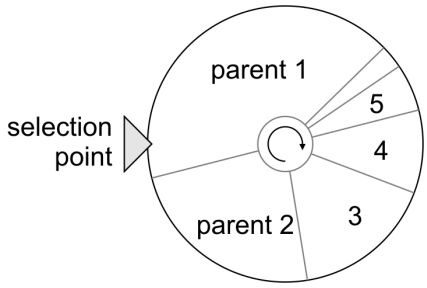

Fig. 4.1: Roulette-wheel selection.

$$p_i = \frac{f_i}{\sum_{j=1}^{N} f_j}. \tag{4.23}$$

Arithmetic Crossover is a common way to combine two parent configurations $\mathbf{p}^1$ and $\mathbf{p}^2$ to produce two descendant configurations $\mathbf{d}^1_{unmutated}$ and $\mathbf{d}^2_{unmutated}$:

$$\begin{aligned} \mathbf{d}^1_{unmutated} &= a\mathbf{p}^i + (1-a)\mathbf{p}^j \\ \mathbf{d}^2_{unmutated} &= (1-a)\mathbf{p}^i + a\mathbf{p}^j \end{aligned} \tag{4.24}$$

a is a number chosen randomly between [0.8...1]. The process of arithmetic crossover is repeated until the defined number of children is reached.

Mutation additionally varies the population in each generation by adding a vector $\mathbf{v}$, whose elements have a Gaussian distribution, to the parent or already recombinated descendant.

The mean value of the distribution is always zero while the standard deviation σ is a very important and variable parameter. The so called step width σ plays a key role for convergence stability and speed of the optimization algorithm. Methods for step size adaptation will be described later.

Selection is necessary to limit the population size. Some evolution strategies produce more descendants than number of parents was before. The best or fittest descendants should become the next parents since they obviously have better traits.

Types of Evolution Strategies

Taking parents into account in the selection process, too, the lifetime of each individual can increase to infinity or to the maximum number of generations, respectively. Furthermore, no deterioration is possible, which can be a drawback for global optimization. This type of strategy is called a "+" (in words: "plus") strategy, while selecting new parents from descendants only is a "," (in words: "comma") strategy. A $(\mu + \lambda)$ strategy e.g. means, that the initial population size is μ individuals which produce λ descendants and the best μ of all $(\mu + \lambda)$ become the parents in the next generation.
Some different types of evolution strategies where established and one has to decide, which one is the best for the current problem. In this work the $(\mu/\rho, \lambda)$ was used for the parameter identification and will be described in detail.

4.2.2.2 $(\mu/\rho, \lambda)$ Evolution Strategy

The $(\mu/\rho, \lambda)$ ES (in words: μ over ρ comma λ) is a higher order evolution strategy where μ is the number of parental configurations, ρ is the number of parents used for recombination and λ is the number of descendants. In each generation ρ individuals are chosen from the μ individuals by roulette-wheel selection and are acting as the only parents of all descendants in this generation. A block diagram of the complete strategy is shown in Fig. 4.2.

The algorithm starts with a set of μ initial parameter configurations that is produced randomly. The initial step width can be chosen by a certain percentage of the parameter

range of each parameter separately (e.g. 15%). Then ρ individuals are chosen by roulette wheel selection, where fitness is taken into account. λ descendants are produced by recombination of the ρ parents. To give variation to the descendants, mutation must be applied to them by adding a normally distributed vector. The standard deviation or step width σ of the normal distribution must be controlled during the strategy to provide stability and an adequate convergence speed. $\boldsymbol{\sigma}$ is inherited from parents to descendants in the recombination step but changes before mutation is performed. For each descendant it is randomly decided if the step width vector $\boldsymbol{\sigma}$ is multiplied or divided by a factor α:

$$\alpha\boldsymbol{\sigma} \quad \text{or} \quad \frac{1}{\alpha}\boldsymbol{\sigma} \tag{4.25}$$

α should be a scalar value between 1.05 and 1.2. The higher α is chosen, the faster the algorithm converges but maybe fails to reach the global solution on the costs of speed. Therefore it is strongly necessary to observe the strategy behavior related to convergence and quality before deciding for a certain α value.
Once all descendants are built, the objective function is calculated for each individual. Due to the functional given in (4.8), the objective function can be defined in a least squares sense by minimizing the residual between measured data and the forward solution.

Stopping Criterion

If the stopping criterion is fulfilled, the strategy stops, otherwise the best (fittest) individuals are the parents of the next generation.
The stopping criterion can be one of the following items or a combination of it:

- The objective function has become smaller than a certain value ε that may be in the order of the assumed noise.
- The change in the objective function has become smaller than $\Delta\varepsilon$.
- The maximum number of function calls or of generations has been exceeded.
- The norm of the population qn (4.26) has become smaller than a prescribed ε_{norm}. This means that the individuals grow together in the parameter space and no more major parameter steps or changes are to be expected.

The population norm qn can be mathematically expressed by

$$qn = \frac{1}{\lambda n} \sum_{j=1}^{n} \sum_{i=1}^{\lambda} \left(\frac{x_{j,i} - \bar{x}_j}{\bar{x}_j} \right)^2 \tag{4.26}$$

with n being the number of parameters, λ is the number of descendants, $x_{j,i}$ is the jth parameter of the individual i and $\bar{x}_j$ is the mean parameter value over all individuals.

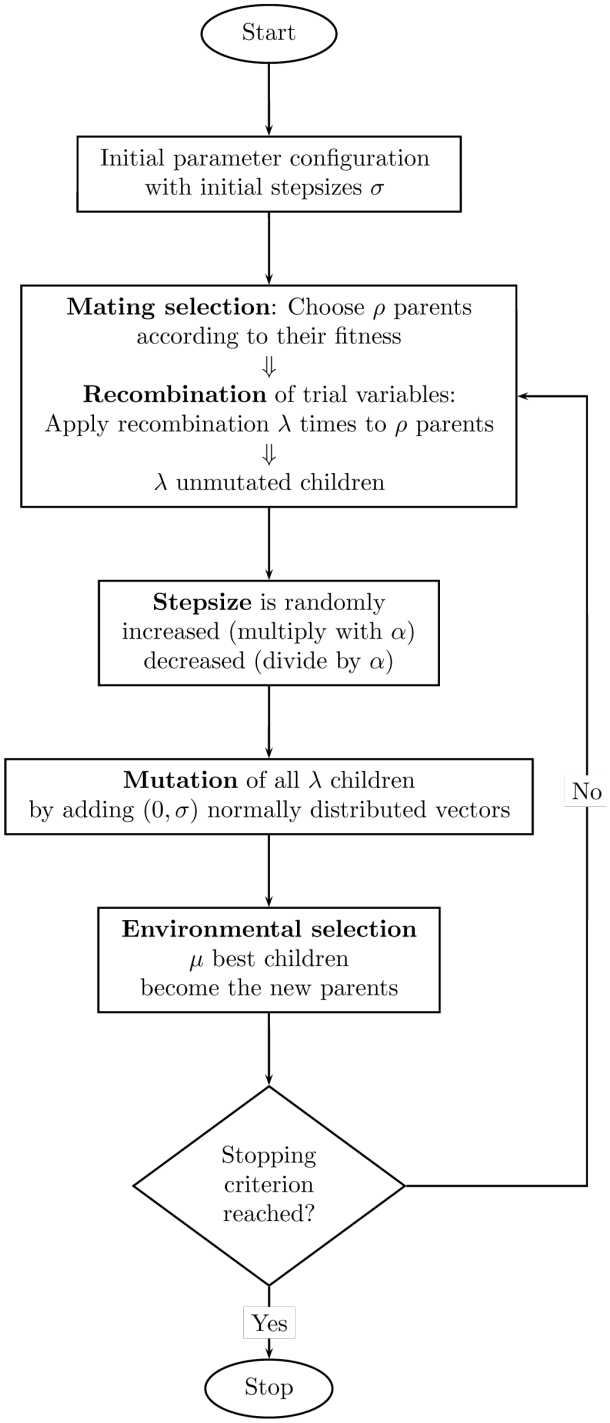

Fig. 4.2: Algorithm of the $(\mu/\rho, \lambda)$ Evolution Strategy.

5 Identification Results

Identification in the sense of the current problem means to detect the positioning parameters of a hidden conductive object, namely a conductive ring, by using magnetic field measurements at a relatively large distance from the ring.

A deterministic as well as a stochastic method was applied to solve the non-linear ill-posed inverse problem. A comparison concerning the accuracy and identification time of the two methods is shown in this chapter. Furthermore, it is shown how the advantages of both approaches can be combined to speed-up the convergence and to improve the robustness of the identification process.

The measurement configuration is identical for all investigations. 8 GMR sensors are located in an equidistant manner along a ring (see Fig. 5.2). The orientation of the axis of sensitivity of each GMR sensor coincides with the radial direction at the position of the respective GMR, assuming the origin in the center of the ring. Three of these sensor layers are placed in y-direction (Fig. 5.1). The parameters are the position of the conductive ring (x, y, z) and the two angles describing the orientation (defined as rotation ϑ and inclination φ), as shown in Fig. 5.3, and the parameter space is restricted by the constraints given in Table 5.1. The measured magnetic field $\mathbf{B}_t$ is the sum of the unperturbed field $\mathbf{B}_s$ and the magnetic field produced by eddy currents in the conductive object $\mathbf{B}_{ed}$. Since the sensor positions do not change relative to the excitation coils, the unperturbed field is constant and can be neglected in simulations when solving the inverse problem. However, when data noise is considered, a relative noise level of the total field has to be taken into account.

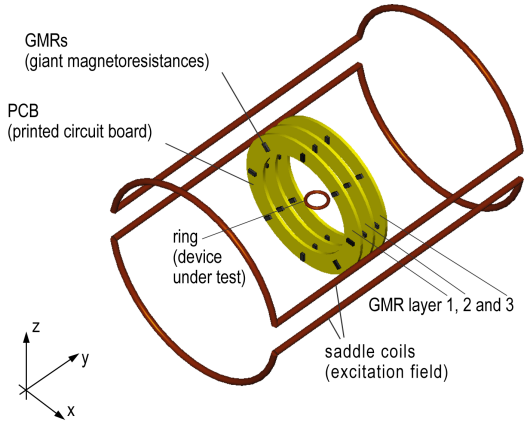

Fig. 5.1: Schematic measurement configuration with all relevant components for the simulation.

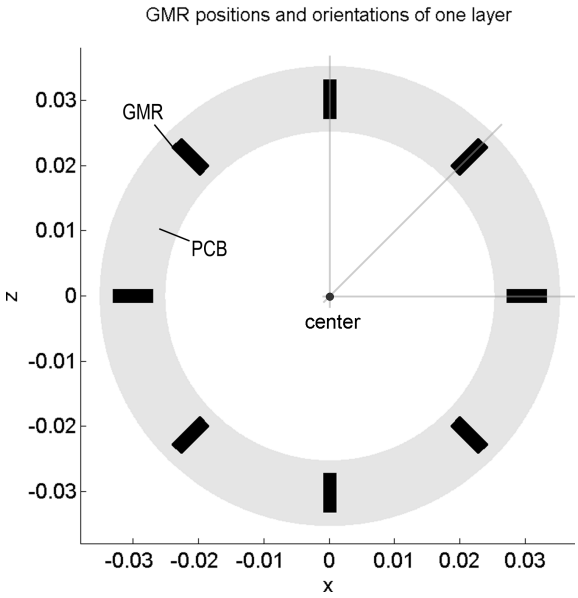

Fig. 5.2: Front view of the radial configuration of GMR sensors on a ring-shaped printed circuit board.

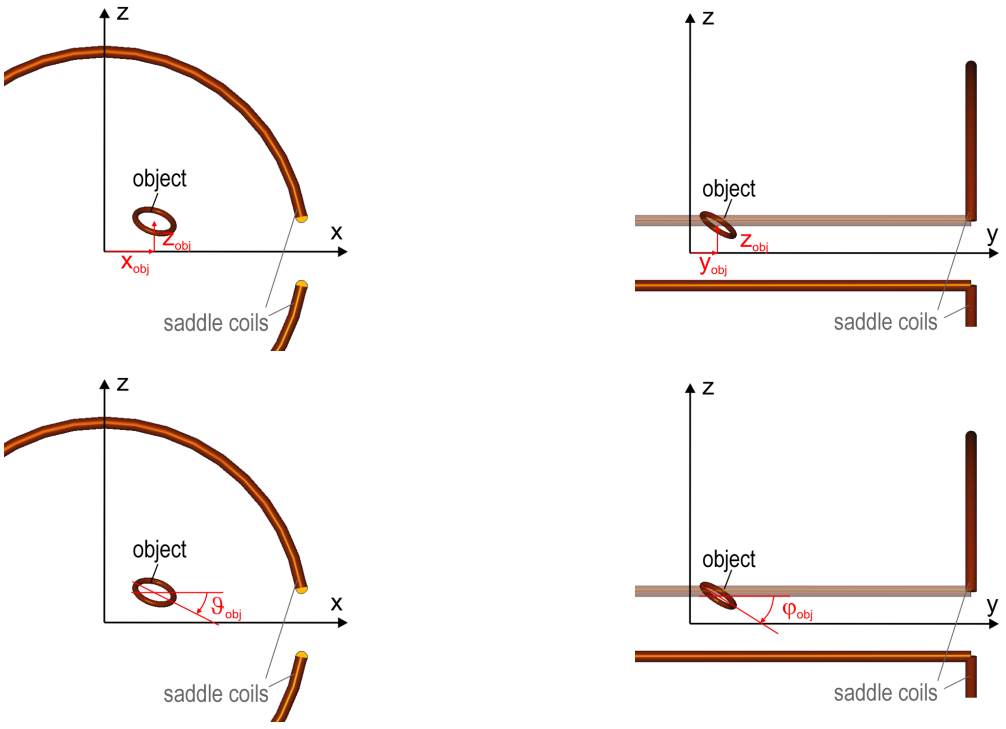

Fig. 5.3: Definition of the object parameters $(x, y, z, \vartheta, \varphi)_{obj}$.

Table 5.1: Object parameter constraints.

	x in mm	y in mm	z in mm	ϑ in °	φ in °
min	-20	-20	-20	-10	-10
max	20	20	20	10	10

5.1 Identification with the Iteratively Regularized Gauss-Newton Method

The equation, as described in Section 4.2.1.4,

$$\left(\mathrm{J}(\mathbf{x})^{\mathsf{T}}\mathrm{J}(\mathbf{x}) + \alpha \mathrm{L}^{\mathsf{T}}\mathrm{L}\right)\mathbf{p}_k = -\mathrm{J}(\mathbf{x})^{\mathsf{T}}\mathbf{r}(\mathbf{x}) + \alpha \mathrm{L}^{\mathsf{T}}\mathrm{L}\left(\mathbf{x} - \mathbf{x}_0\right) \tag{5.1}$$

has to be solved in each iteration step. $\mathrm{J}(\mathbf{x})$ denotes the Jacobian matrix, $\mathbf{y}^{\delta}$ is the noisy measurement data vector and $\mathbf{x}_0$ is the initial guess or a-priori knowledge about the solution or any assumed starting value, otherwise. Furthermore, L is the regularization matrix and α is the regularization parameter. $\mathrm{J}(\mathbf{x})$ is the numerically approximated gradient of $\mathrm{F}(\mathbf{x})$ which means that in each iteration the forward problem has to be solved 11 times (once for $\mathrm{F}(\mathbf{x})$ and 2 times 5 for the gradients since outer differences are used).

5.1.1 Evaluation of the Regularization Parameters

As described in section 4.2.1.3, finding an appropriate sequence for α is important for the stability and convergence, although it is very difficult to find. The method of trial and error was used to determine the regularization parameter sequence as good as possible for many different parameter sets.

But first, the regularization matrix L has to be defined. In the easiest case, i.e. considering equal dimensions and sensitivities for all parameters, the identity matrix can be used. Unfortunately, both is not the case in the present inverse problem:

- The dimension of the positioning parameter x, y, z is meter, while the angles are given in degree. Considering the full range between upper and lower parameter constraints, the ratio of positioning to angle parameters is $\frac{0.04\,\mathrm{m}}{20^\circ} = 2 \cdot 10^{-3}\ \frac{\mathrm{m}}{^\circ}$.
- The sensitivity is about 4 decades lower for the angles than for the positioning parameters.

Since the regularization factor α is multiplied by $\mathrm{L}^\mathsf{T}\mathrm{L}$, the regularization matrix can be considered as a regularization weighting in each iteration. A compromise between the differing sensitivities and dimensions could be finally found by the matrix:

$$\mathrm{L}^\mathsf{T}\mathrm{L} = \begin{bmatrix} 1 & 0 & 0 & 0 & 0 \\ 0 & 1 & 0 & 0 & 0 \\ 0 & 0 & 1 & 0 & 0 \\ 0 & 0 & 0 & 2 \cdot 10^{-5} & 0 \\ 0 & 0 & 0 & 0 & 2 \cdot 10^{-5} \end{bmatrix} \tag{5.2}$$

For the determination of an appropriate regularization starting value, α_0 was chosen to be 1 initially. An arbitrary parameter set to be identified and the matrix $\mathrm{L}^\mathsf{T}\mathrm{L}$ given in (5.2) were used. α was decreased by multiplying it with a factor $f_\alpha = 0.1$ in each iteration and the results obtained with these assumptions are shown in Fig. 5.4 and 5.5.

Up to iteration 10 no significant change in the parameters and the residual norm can be observed. That means that the regularization is too strong and therefore the starting value can be decreased. Since a remarkable change happens after 10 iterations, α_0 can be set to 10^{-10} $(= 1 \cdot 0.1^{10})$ from the very beginning. Doing so, the algorithm starts in the first iteration with major parameter changes in the correct directions (Fig. 5.6) and convergence is given within 17 iterations with a relative parameter error of less than 1% of the full parameter range (i.e. 0.4 mm and 0.2°). The relative parameter error e_p is the maximum value of the relative parameter error vector:

$$\begin{aligned} \Delta\mathbf{p}_{rel} &= \frac{|\mathbf{p}_{true} - \mathbf{p}_{identified}|}{\mathbf{p}_{max} - \mathbf{p}_{min}} \\ e_p &= \max\left(\Delta\mathbf{p}_{rel}\right) \end{aligned} \tag{5.3}$$

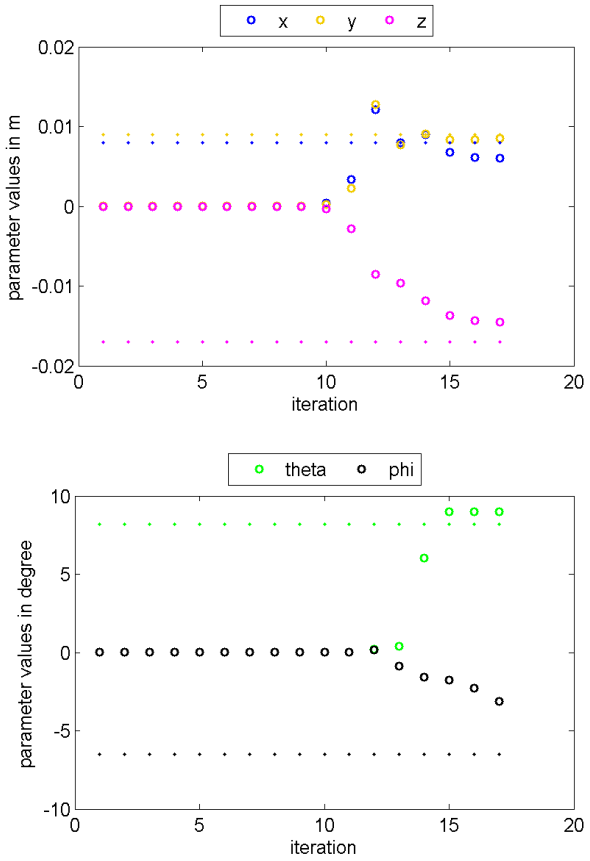

Fig. 5.4: Parameter characteristics of the Iteratively Regularized Gauss-Newton algorithm with $\alpha_0 = 1$ and $f_\alpha = 0.1$

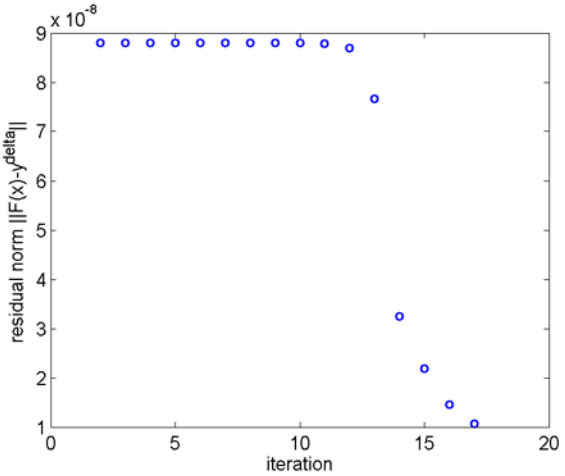

Fig. 5.5: Residual norm characteristics of the Iteratively Regularized Gauss-Newton algorithm with $\alpha_0 = 1$ and $f_\alpha = 0.1$

On the contrary, the relative parameter accuracy in % is $100\%\,(1 - e_p)$.

It can be observed that the positioning parameters are identified at iteration 15, while the angle parameters converge a bit slower. This observation corresponds to the lower sensitivity of the angle parameters.

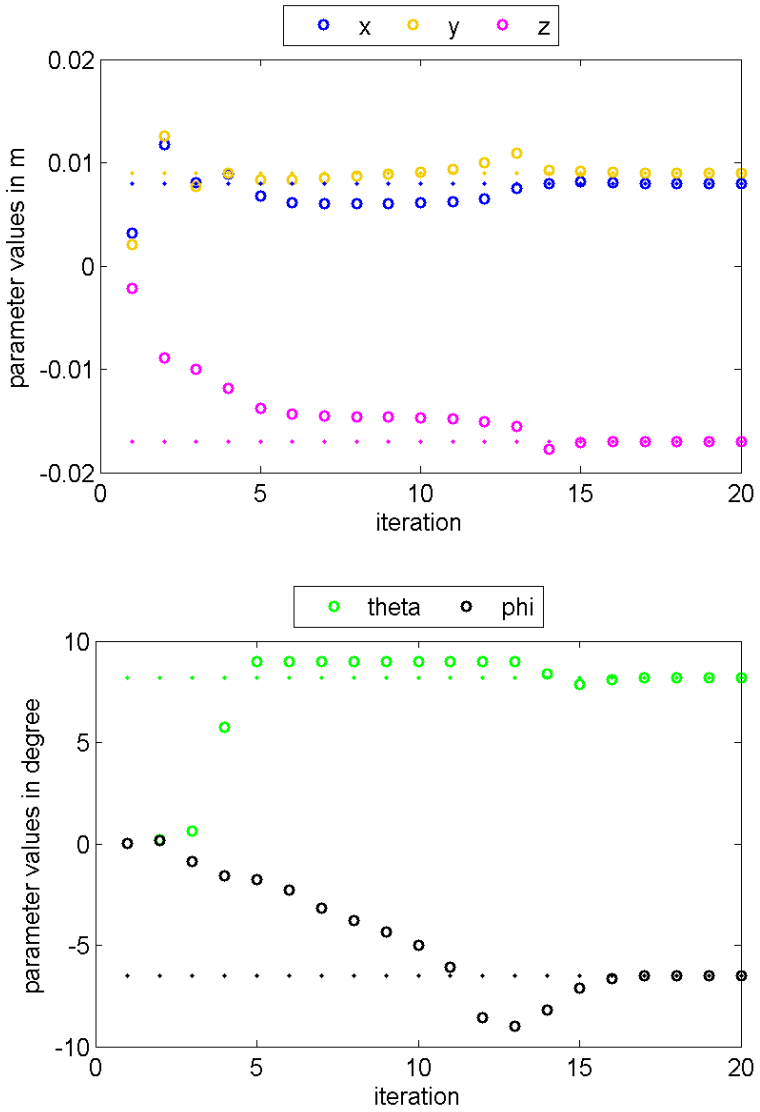

Fig. 5.6: Parameter characteristics of the Iteratively Regularized Gauss-Newton algorithm with $\alpha_0 = 10^{-10}$ and $f_\alpha = 0.1$

5.1.2 Results

First of all, 100 different parameter sets to be identified were assumed to check the success rate of the identification process with the deterministic Iteratively Regularized Gauss-Newton algorithm. The used configuration and algorithm parameters are summarized here:

- Measurement configuration as shown in Fig. 5.1 with 3 x 8 GMR sensors in radial configuration.
- Initial parameter set $\mathbf{x}_0 = (0, 0, 0, 0, 0)$.
- Regularization parameters: $\mathrm{L}^\mathsf{T}\mathrm{L} = \mathrm{diag}(\mathbf{l})$ with $\mathbf{l} = (1, 1, 1, 2 \cdot 10^{-5}, 2 \cdot 10^{-5})$; $\alpha_0 = 10^{-10}$, $f_\alpha = 0.1$.
- Parameter constraints as stated in Table 5.1.
- e_p as defined in (5.3).

For the first investigations data noise was neglected and the stopping criterion was defined to stop if the parameter error e_p is below 1% or if a maximum number of iterations (50 in this case) is reached. In fact, applying the algorithm in practice requires a criterion bound to the measurement quantities. The correlation of the parameter error to the output residual norm has been investigated and is shown later in this section.
10 of 100 parameter sets could not be identified with a parameter error $< 5\%$ and therefore the success rate is 90% for this accuracy limit. Fig. 5.7 gives an overview on the success rate characteristic as a function of the relative parameter error. The mean iteration number of identification results with $e_p < 1\%$ is 6.43. Thus, the number of function calls needed to identify an object position is 71 on average. The same investigations were done considering different data noise levels and the summarized results are shown in Table 5.2. Here, data noise is defined by a gaussian distribution with a standard deviation denoted as noise level. The table of results shows that the 99% accuracy is reachable with very low noise only.

It is well known that the success of Gauss-Newton methods depends on the choice of the initial parameter vector. To investigate whether a large distance between the initial and the true parameter set is the cause for failing with the Iteratively Regularized Gauss-Newton algorithm, all of the 100 solutions are illustrated as a function of the distance

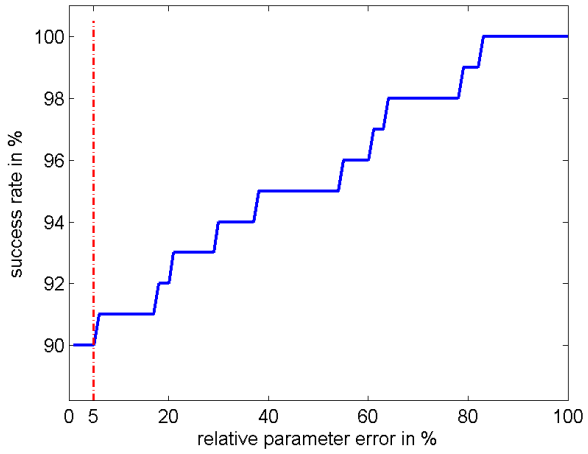

Fig. 5.7: Success rate as a function of the parameter accuracy, neglecting data noise. 90% of all parameter sets have a relative parameter error below 5%.

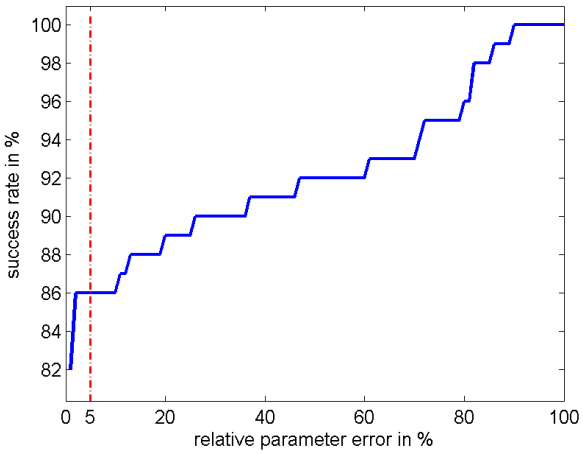

Fig. 5.8: Success rate as a function of the parameter accuracy for noisy data (noise level of 1 nT). 86% of all parameter sets have a relative parameter error below 5%.

Table 5.2: Results of the parameter identification with the Iteratively Regularized Gauss-Newton algorithm.

	success rate in %		nr. of iterations		function calls
	error $< 1\%$	error $< 5\%$	mean	max.	mean value
no data noise	90	90	6	12	71
noise level: 0.1 nT	82	86	7	25	75
noise level: 0.5 nT	20	77	6	18	67
noise level: 1 nT	8	61	6	10	65

$d_i = |p_{i,true} - p_{i,0}| = |p_{i,true}|$ for $\mathbf{p}_0 = (0, 0, 0, 0, 0)$ in Fig. 5.9. It can be seen that the above assumption (large distance - less successful) is true in case of the positioning parameters x, y and z while the outliers of the angle parameters are more or less equally distributed. The higher number of outliers for φ and ϑ are again explainable by the lower sensitivity. This means that the maximum number of iterations is reached before the angle parameters converged. Assuming a noise level of 0.1 nT, this effect is even more clearly (see Fig. 5.10).

Monitoring the parameter accuracies is an appropriate way to investigate the behavior and quality of the identification process. However, the true parameter set is not available in practice and therefore the residual between the measurement values (simulated or measured)

and the forward problem solution has to be evaluated. Of course, the goal is to minimize the residual but, unfortunately, it may happen that the measurement system is badly configured (e.g. by a disadvantageous choice of the sensor positions and orientations) and hence one or more parameters have none or a very small effect on the residual norm $\|\mathbf{r}\| = \left\|\mathrm{F}(\mathbf{p}) - \mathbf{y}^{\delta}\right\|$. In Fig. 5.11 the correlation between the parameter accuracy and the residual norm is shown. Here, a parameter vector $\mathbf{p} = (x, y, z, \vartheta, \varphi)$ was perturbed by a certain percentage in one single parameter direction and the change of the residual norm Δr due to the parameter change was calculated. For instance, perturbing the parameter x by n percent of the parameter range Δx,

$$
\begin{aligned}
x_1 &= x - \frac{1}{2}\, n\,(0.01\,\Delta x) \\
x_2 &= x + \frac{1}{2}\, n\,(0.01\,\Delta x) \\
&\text{with} \\
\Delta x &= x_{max} - x_{min}, \qquad (5.4)
\end{aligned}
$$

the residual norm $\|\mathbf{r}\|$ can be calculated in $\mathbf{p}_1$ and $\mathbf{p}_2$:

$$
\begin{aligned}
\|\mathbf{r}_1\| &= \|\mathrm{F}(\mathbf{p}_1) - \mathbf{y}\| \\
\|\mathbf{r}_2\| &= \|\mathrm{F}(\mathbf{p}_2) - \mathbf{y}\| \\
\Delta r &= \|\mathbf{r}_2\| - \|\mathbf{r}_1\|\,. \qquad (5.5)
\end{aligned}
$$

It can be seen again, that the positioning parameters are more affecting on the residual than the angle parameters. Furthermore, ϑ and φ are the critical parameters concerning data noise. That means that noise must not be greater than the smallest residual norm, which is 0.6 nT for the considered parameter states and 99% parameter accuracy.

In fact, the Iteratively Regularized Gauss-Newton method is quite fast with only about 70 function calls. Nevertheless, the desired accuracy can not be achieved in all cases and hence a more robust method has to be found.

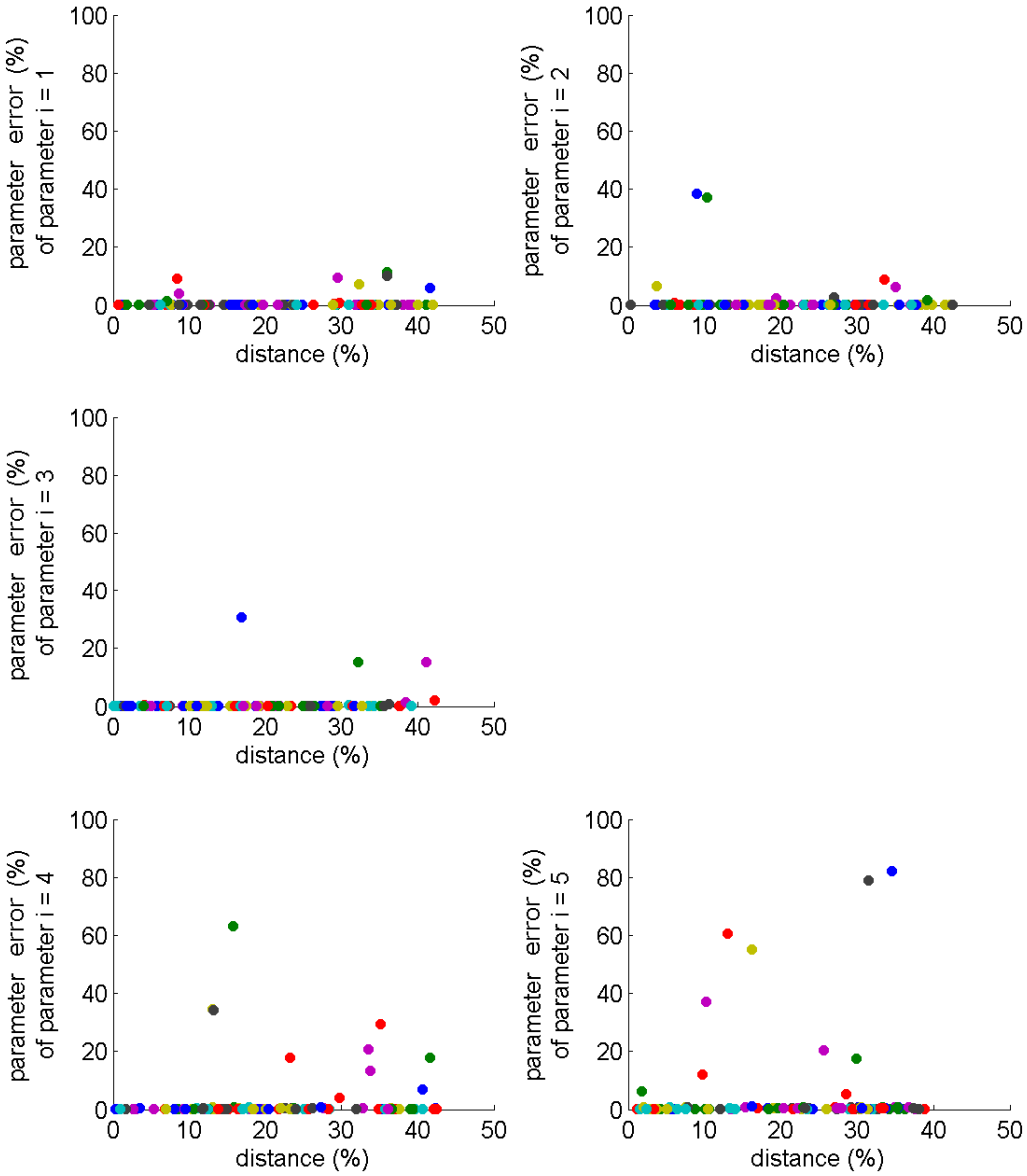

Fig. 5.9: Relation between the relative parameter error and the distance between the initial and the true parameter set. i is the index of the parameter vector $(x, y, z, \vartheta, \varphi)$.

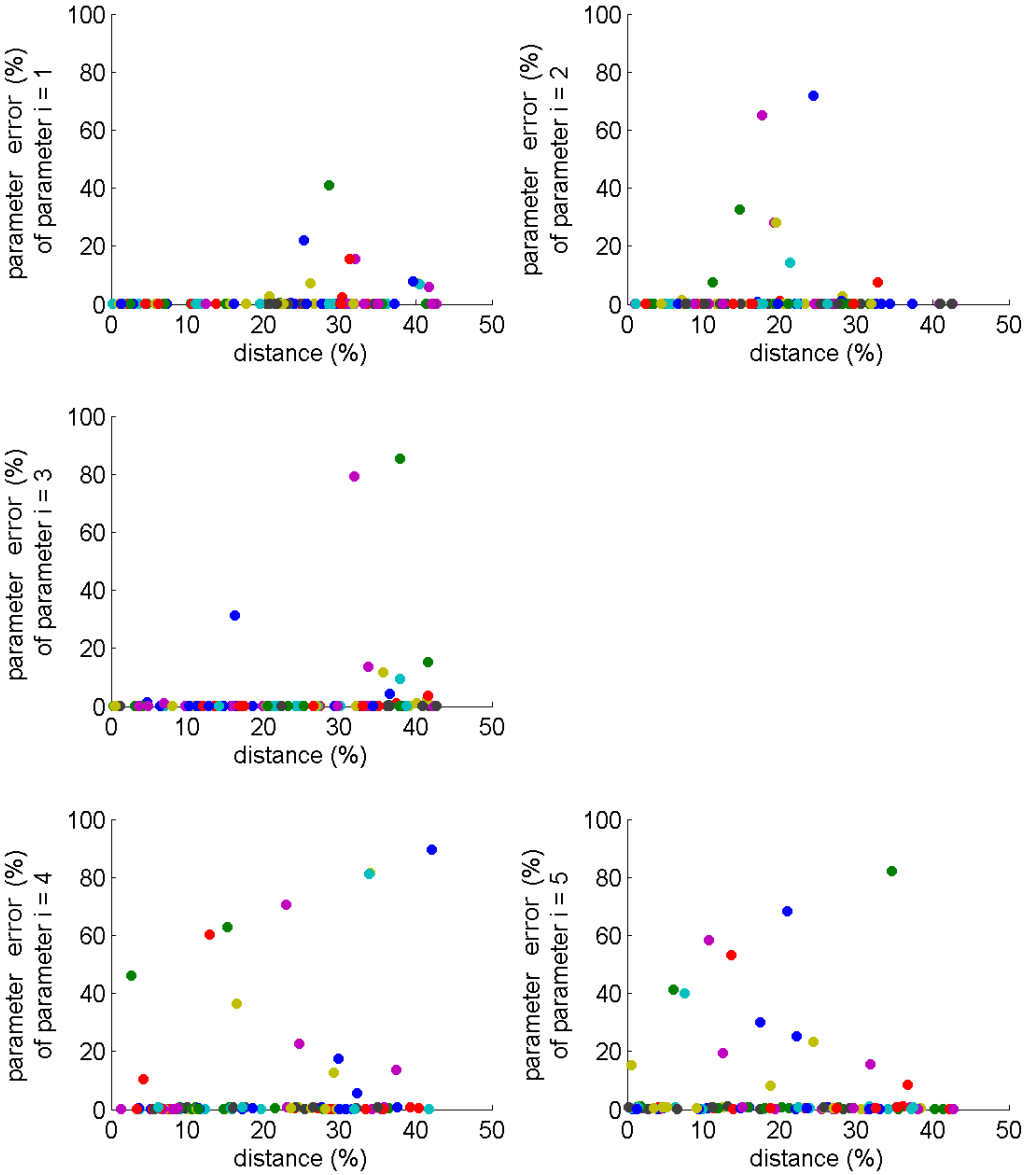

Fig. 5.10: Relation between the parameter accuracy and the distance between the initial and the true parameter set. i is the index of the parameter vector $(x, y, z, \vartheta, \varphi)$. A data noise level of 0.1 nT was assumed in this calculations.

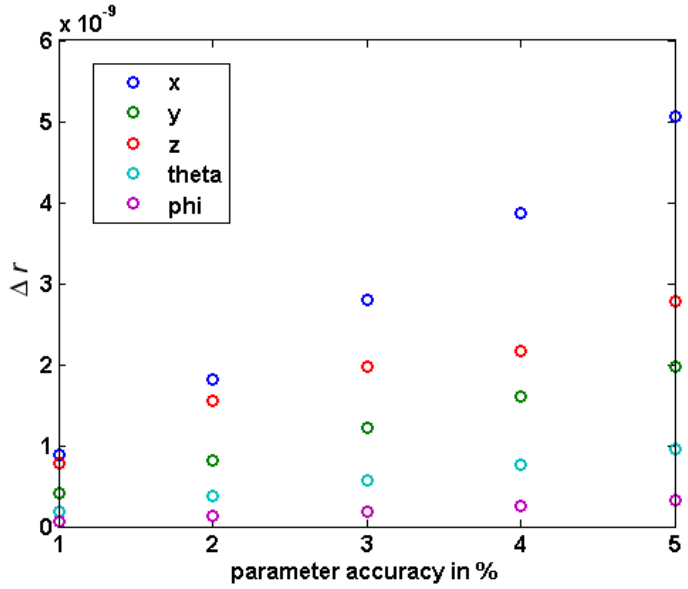

Fig. 5.11: The residual norm of 20 different parameter sets were evaluated for parameter errors from 1% to 5%. The mean values of the residual norm are plotted for each parameter seperately.

5.2 Identification with the $(\mu/\rho, \lambda)$ Evolution Strategy

The main strategy parameters of the $(\mu/\rho, \lambda)$ Evolution Strategy are the population size μ, the number of parents ρ and the number of descendants λ. In addition to these parameters the initial step width σ_0, the step width variation factor α and appropriate stopping criteria for the problem in hand have to be found. In this section the choices of the used strategy parameter are illustrated first and the corresponding results are shown. With some modifications of the standard $(\mu/\rho, \lambda)$ Evolution Strategy and refinements of the initial strategy parameters, the identification results could be improved and are shown in this section, too.

5.2.1 Choice of the Strategy Parameters

The challenge of choosing appropriate values for the main strategy parameters is realizing a high convergence speed while maintaining the global behavior of the optimization algorithm. λ is the decisive parameter since it is proportional to the number of function calls needed in each generation. Increasing λ means to increase the computation time, decreasing it may lead to a local behavior of the strategy. Of course, μ and ρ also play an important role for the accuracy but they fairly affect to the computation time only in a very small manner compared to the number of descendants λ. The parental population size μ preserves the diversity of the population and is therefore crucial for the global minimization result.
The population size was chosen with $\mu = 8$, which means a good coverage of the whole parameter space in general. Two parents are chosen out of all population individuals by roulette wheel selection, i.e. the fitness of the individuals is taken into account. Using the rule of thumb for the λ to μ ratio of about 2-3, λ was set to 20. Thus, a $(8/2, 20)$ Evolution Strategy was used for the stochastic identification algorithm.

5.2.2 Application of the Standard $(\mu/\rho, \lambda)$ Evolution Strategy

A representative run of a $(8/2, 20)$ Evolution Strategy, which is described in Section 4.2.2.1 and has been applied to the problem in hand, is shown in Fig. 5.12. An initial step width of 30% of the parameter range was chosen. The parameter diagrams, that are split in two pictures, show the best 8 out of $\lambda = 20$ descendants of each generation, which are to become the new

μ parents. The best solution in each generation is highlighted. The actual parameters that have to be identified were assumed to be $(x, y, z, \vartheta, \varphi)_{obj} = (-7\,\text{mm}, 1.4\,\text{mm}, 8\,\text{mm}, 9\,°, -8\,°)$.

In fact, the convergence of the algorithm is apparent, but unfortunately it converges to the

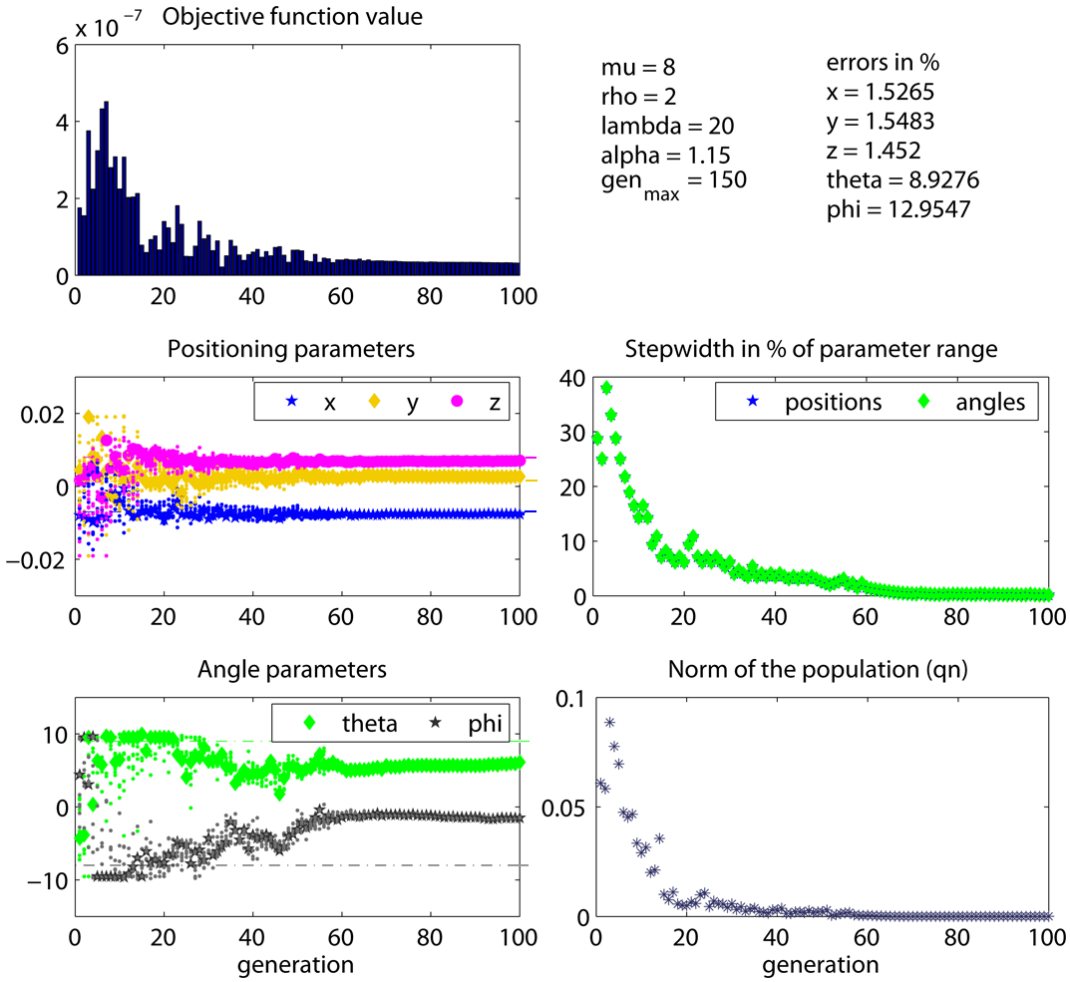

Fig. 5.12: Characteristic diagrams of a standard $(8/2, 20)$ Evolution Strategy. The dashed-dotted lines in the parameter diagrams depict the true values. The step width as well as the population norm decrease very fast (within 20 generations). The best value was found in generation 33 where the positioning parameters are more or less identified. Nevertheless, the algorithm tends to another solution concerning the angle parameters.

wrong solution. The positioning parameters x, y, z are identified with quite some accuracy, while the angles are completely wrong. The objective function seems to be badly conditioned for this model. Additional information must be added to obtain a higher sensitivity regarding the angle parameters.

5.2.3 Objective Function Extension by Consideration of Gradients

An improvement in mapping the parameter errors to the objective function can be reached by taking gradients into account. It can be observed that changing the inclination φ of the copper ring results in a signal variation between flux densities in layer 1 and layer 3 (the exterior layers, see Fig. 5.1) in opposite directions. Altering the ring in ϑ-direction causes an opposite signal change inside each layer. Thus, considering this additional information, the objective function can be extended to (5.6), where j and k are the indexes of the corresponding GMR sensors where the particular gradient is taken. A characteristic behavior of the Evolution Strategy with the extended objective function is shown in Fig. 5.13 and points out, how this new objective function virtually improves the convergence behavior of the Evolution Strategy.

$$\begin{aligned} of = & \sum_{i=1}^{n_{GMR}} (B_{i,act} - B_{i,meas})^2 + \\ & + \sum_{j,k} ((B_{j,act} - B_{k,act}) - (B_{j,meas} - B_{k,meas}))^2 + \\ & + \sum_{p,q} ((B_{p,act} - B_{q,act}) - (B_{p,meas} - B_{q,meas}))^2 \end{aligned} \tag{5.6}$$

with

$$\begin{aligned} j &= \left(1, \ldots, \frac{ngmr}{3}\right) \\ k &= \left(\frac{2\,ngmr}{3} + 1, \ldots ngmr\right) \\ p &= \left(1, \ldots, \frac{ngmr}{6}, \frac{ngmr}{3} + 1, \ldots, \frac{ngmr}{2}, \frac{2\,ngmr}{3} + 1, \ldots, \frac{5\,ngmr}{6}\right) \\ q &= \left(\frac{ngmr}{3}, \ldots, \frac{ngmr}{6} + 1, \frac{2\,ngmr}{3}, \ldots, \frac{ngmr}{2} + 1, ngmr, \ldots, \frac{5\,ngmr}{6} + 1\right) \end{aligned}$$

Especially the accuracy of finding the angle ϑ could be improved by augmenting the objective function and locks in the correct value a few generations after the positioning parameters converged, nevertheless, φ is still badly identified. The tendency to the actual value is given which means that if the step width would be large enough at this stage of the iterative process (around 40 in Fig. 5.13), this last parameter could also be forced to converge properly. Thus, the $(\mu/\rho, \lambda)$ Evolution Strategy has to be modified in such a way to take these differing

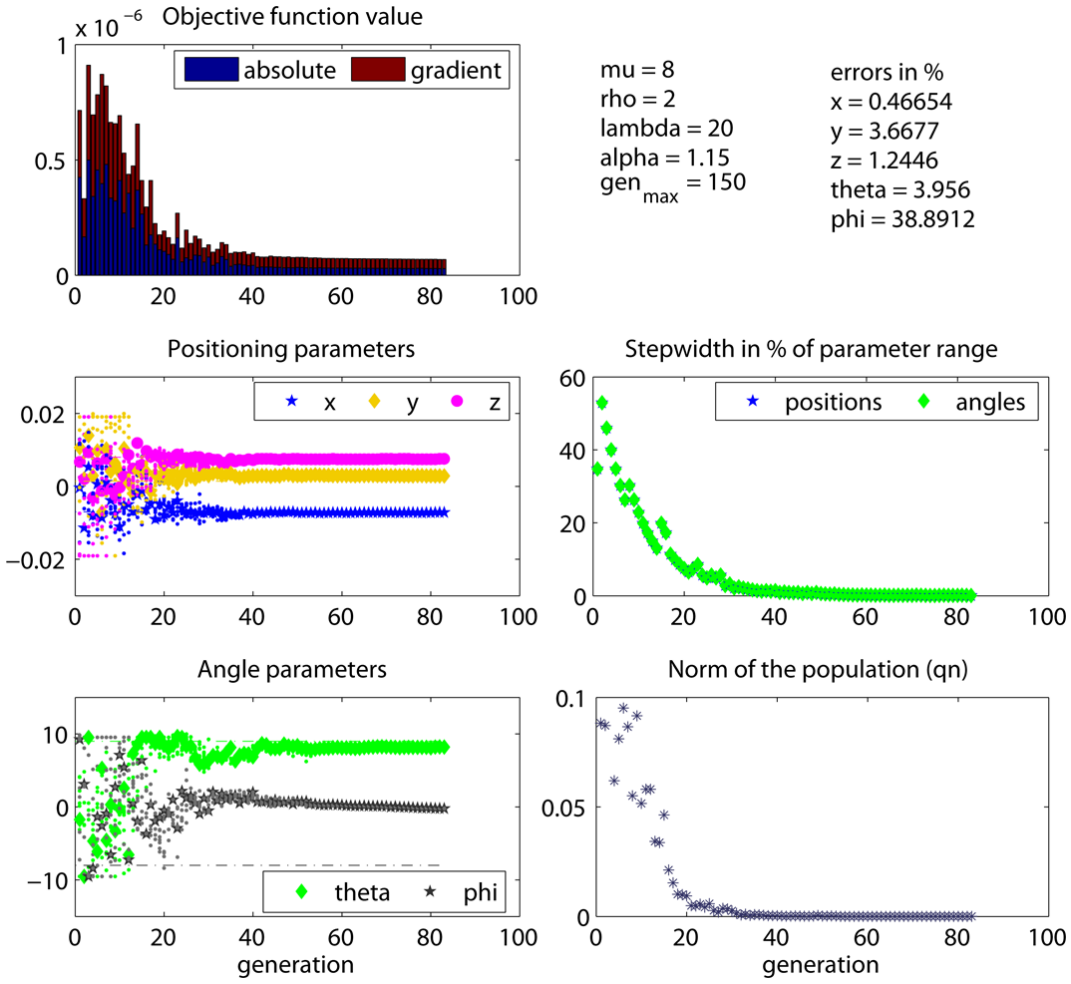

Fig. 5.13: A representative run considering gradients in the objective function additionally. The angle φ tends to the true value starting at generation 40, but the step width and the population norm are already too small.

sensitivities into account.

5.2.4 Initial Step Width Variation

As mentioned before, the step widths of the parameters with low sensitivity must be larger at later generations. This is, when they start contributing a considerable quantity to the objective function. But holding the angle step width constant till the positioning parameters are locked in, the algorithm does not converge. An alternative approach is to choose the initial step widths differently for position and angles. The results of this improvement by

using a four times lower initial step width for x, y, and z are shown in Fig. 5.14.

It can be observed that the algorithm converges into the optimal solution with errors

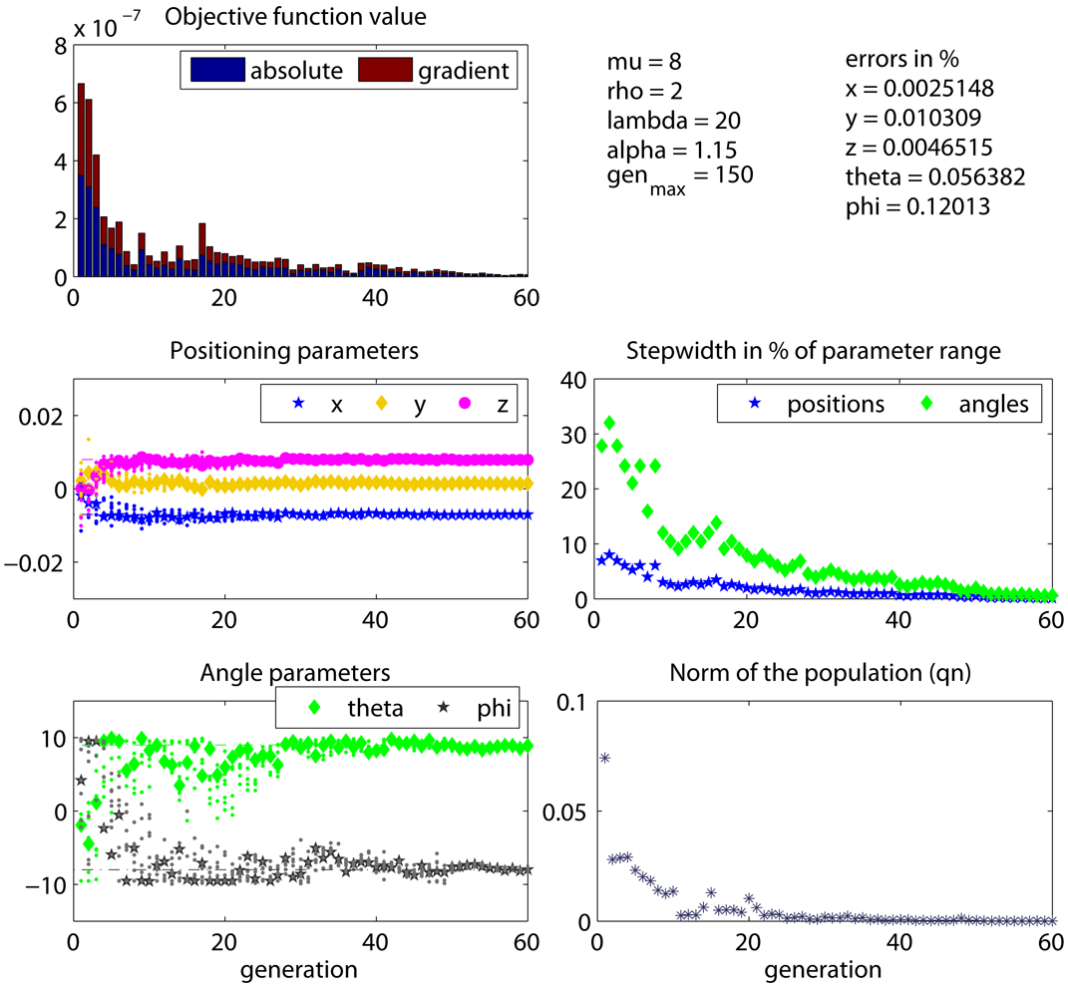

Fig. 5.14: Well identification starting with different initial step widths.

below 1%, whereby the goal of identification is basically reached. Nevertheless, the time of identification plays a crucial role too. Further investigations have to be made for speeding up the identification process. Fortunately, the very small step widths for the positioning parameters lead to a fast decrease of the objective function value within just a few generations and thus the population variance or population norm decreases too. Using the information coming from the population norm is a potential opportunity to speed up the algorithm and will be pointed out in the next lines.

5.2.5 Adaptive Modification of the Step Width Factor α

As mentioned in 4.2.2.1, the step width of each of the parameters is either multiplied with or divided by α in each generation. α is crucial for the convergence speed and the stability of the Evolutions Strategy, but behaves rather locally. This means that the strategy gets trapped very likely in one of the first local solutions detected. Thus, starting with an α near to 1 is important to provide a global behavior. When the individuals of the population grow together, which can be observed in the population norm qn, α can be increased and thus convergence will be accelerated. In Fig. 5.15 the stopping criterion is reached at generation 40 with a comparable relative parameter error.

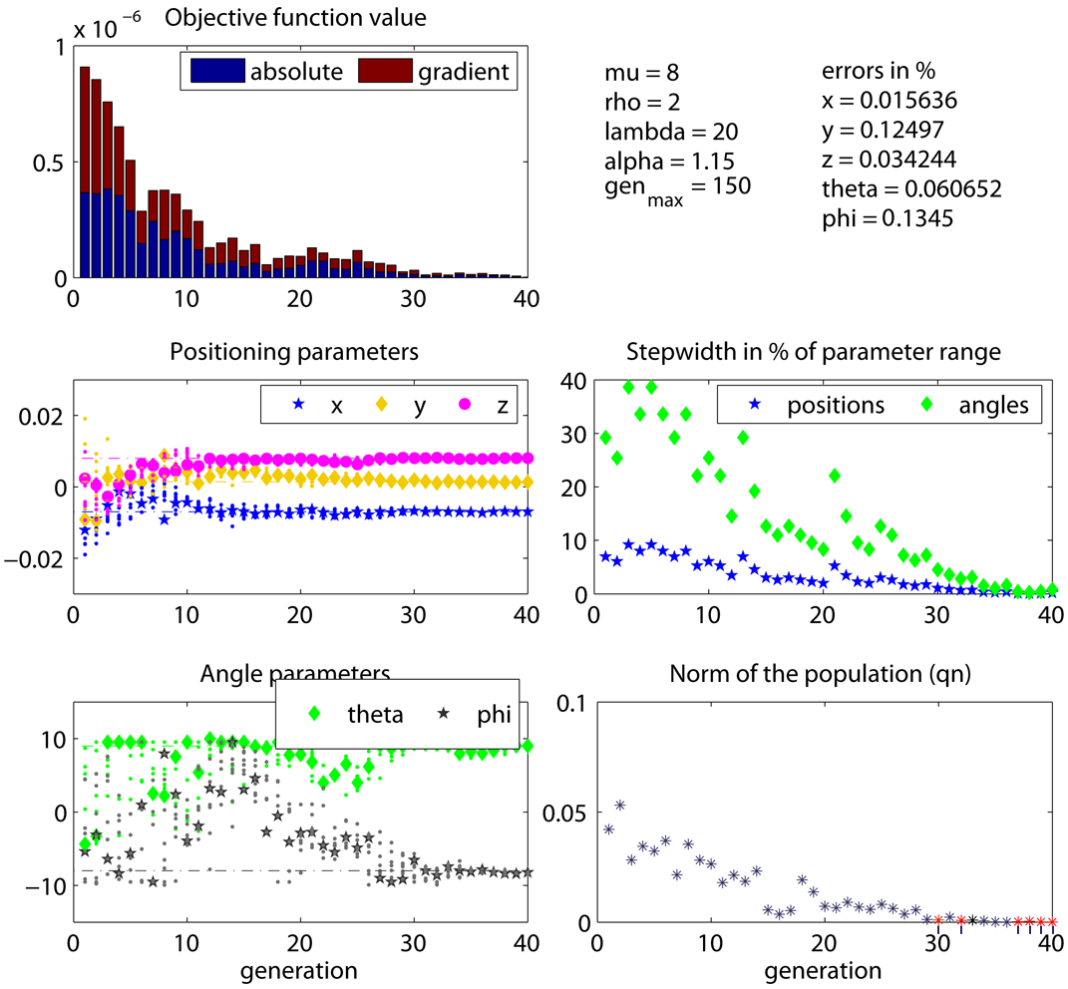

Fig. 5.15: Convergence speedup by adaptive modification of the step width factor α. The ticks on the axis of generations starting at 30 indicate that α has been increased in the corresponding generation.

5.3 Hybrid Identification with Deterministic and Stochastic Methods

As it was shown in the last two sections, the major advantage of the deterministic method is its convergence speed. The number of function calls is about 70 - 100 with a success rate of up to 90% considering a parameter error of below 1%. Unfortunately, the remaining 10% failing the required accuracy will not be appealing to patients and surgeons. On the other hand, the Evolution Strategy provides a success rate near to 100% when considering at least 3 different runs with about 800 - 1000 function calls each. Thus, the idea is to combine the deterministic and the stochastic method and to take advantage of the benefits and to reduce the drawbacks of both approaches.

Performing the deterministic Iteratively Regularized Gauss-Newton method, two facts can be observed when solving the problem at hand:

- The higher the distance between the initial positioning parameters and the true positioning parameters (x, y, z), the higher is the failure rate of the Iteratively Regularized Gauss-Newton algorithm. This is a general feature in solving inverse problems and can be minimized by providing prior information.
- Although the positioning parameters are well identified, the angle parameters may converge to a local solution.

The first fact could be improved by trying to obtain a-priori information with the stochastic algorithm since the results of the Evolution Strategy show a very fast and accurate convergence of the position parameters (but not of the angle parameters).
Attaching an Evolution Strategy to the deterministic algorithm when the required residual is not reached with the Iterativel Regularized Gauss-Newton method, should increase the success rate to 100%. The block diagram of the hybrid identification process is shown in Fig. 5.16.

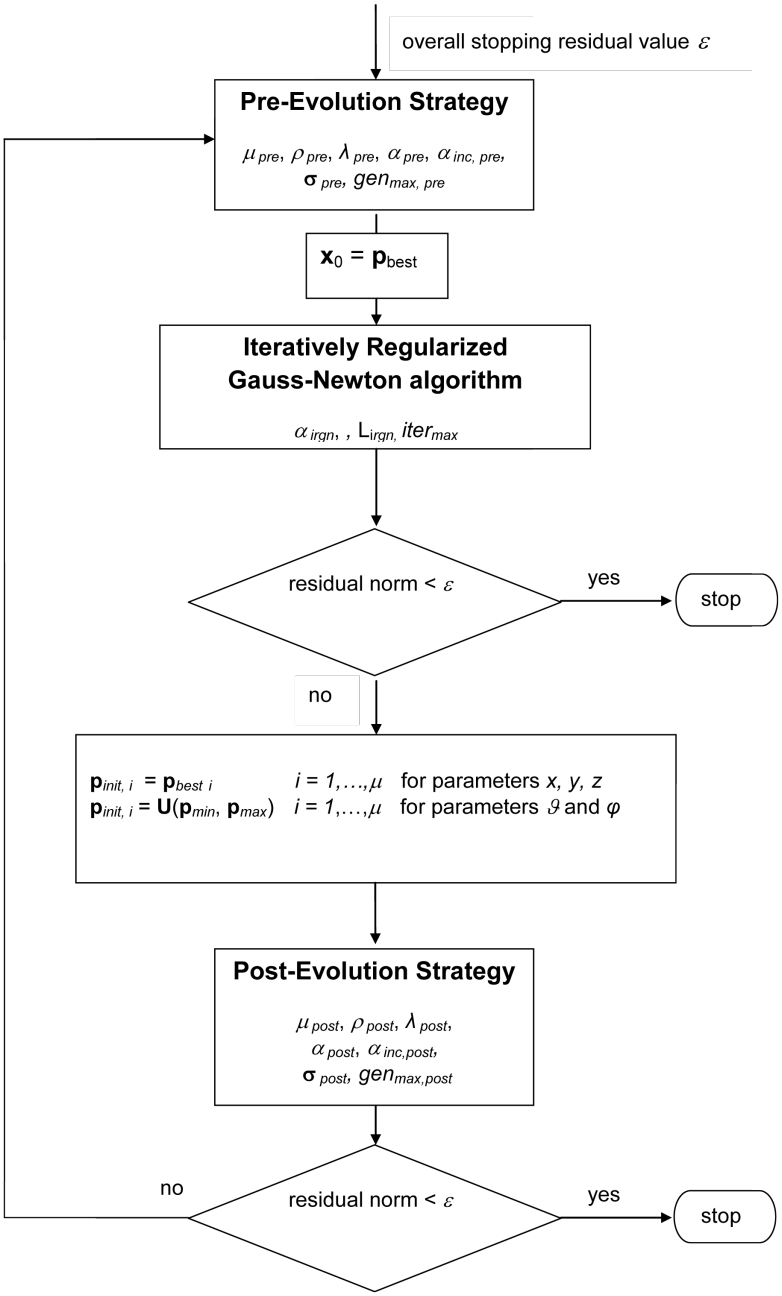

Fig. 5.16: Block diagram of the hybrid identification process.

5.3.1 Obtaining Prior Information by Evolution Strategies

An $(8/2, 20)$ Evolution Strategy, termed Pre-Evolution Strategy, with a low number of generations gen_{max} was applied to obtain the starting values for the deterministic identification algorithm. To determine an appropriate value for gen_{max}, the mean and the worst accuracy values of the best parameters found within gen_{max} are given in Table 5.3. 20 different parameter sets were used for this investigation.

The mean accuracy value within 7 generations is quite good, however, the computation time

Table 5.3: Position parameter errors in % of the parameter range within a certain number of generations using an $(8/2, 20)$ Evolution Strategy.

	$gen_{max} = 5$ 108 funct. calls			$gen_{max} = 6$ 128 funct. calls			$gen_{max} = 7$ 148 funct. calls		
	x	y	z	x	y	z	x	y	z
mean error in %	5.5	8.6	7.2	5.2	7.1	9.0	3.9	3.7	3.7
worst accuracy (error in %)	18.0	27.7	24.0	11.6	25.1	22.0	10.0	7.5	7.6

has to be considered as well. Hence, the deterministic method needs 11 function calls in each iteration while the stochastic method needs λ (= 20 in this case) function calls. Decreasing λ is not advisable since it is even important to preserve variability in the first generations of the Pre-Evolution Strategy. But the accuracy within 5 generations is sufficient and the afterwards launched Iteratively Regularized Gauss-Newton algorithm is able to compensate the remaining parameter differences in about half of the time (11 function calls are needed instead of 20 in the Evolution Strategy). Thus, 5 generations are defined for the Pre-Evolution Strategy part of the hybrid algorithm.

5.3.2 Iteratively Regularized Gauss-Newton Part of the Hybrid Identification Process

The regularization parameters α_0, L and $\Delta\alpha$ are the same as in the single deterministic process described in Sec. 5.1: $\mathrm{L}^{\mathsf{T}}\mathrm{L} = \mathrm{diag}(\mathbf{l})$ with $\mathbf{l} = (1, 1, 1, 2 \cdot 10^{-5}, 2 \cdot 10^{-5})$; $\alpha_0 = 10^{-10}$, $f_\alpha = 0.1$.

The initial parameter state $\mathbf{x}_0$ is taken from the best individual of the Evolution Strategy. The algorithm stops if a certain residual norm ε is reached, otherwise another Evolution Strategy process (Post-Evolution Strategy) is started after a maximum number of iterations $iter_{max}$ of the Iteratively Regularized Gauss-Newton method.

5.3.3 Post-Evolution Strategy for Angle Parameter Detection

Since the positioning parameters (x,y,z) are highly accurate identified after the deterministic part with high accuracy, the step width of these parameters $(\sigma_x, \sigma_y, \sigma_z)$ are set to a very low value. Additionally, the same positioning parameters are used for all μ individuals of the initial population, while the angle parameters are, as usual, randomly chosen within the constraints, (5.7). The basic Evolution Strategy with a self adapting step width factor α was used as described in Sec. 5.2.5. The Post-Evolution Strategy stops if the residual norm ε is reached, otherwise the hybrid process starts again with the first step (the Pre-Evolution part) after a maximum number of generations $gen_{max,post}$.

$$\begin{aligned} \mathbf{p}_{init,i} &= \mathbf{p}_{best,i} && i = 1, \ldots, \mu \text{ for } x, y, z \\ \mathbf{p}_{init,i} &= \mathrm{U}(\mathbf{p}_{min}, \mathbf{p}_{max}) && i = 1, \ldots, \mu \text{ for } \vartheta, \varphi \end{aligned} \tag{5.7}$$

5.3.4 Results of the Multiple Hybrid Identification Algorithm

Four different algorithm sequences turned out to be qualified for a fast and accurate identification process:

1. pre-ES - IRGN
2. pre-ES - IRGN - post-ES (= 1 cycle)
3. pre-ES - IRGN - post-ES - pre-ES - IRGN
4. pre-ES - IRGN - post-ES - pre-ES - IRGN - post-ES (= 2 cycles)

Basically, an infinite number of cycles (pre-ES - IRGN - post-ES) is allowed, but considering 2 cycles only leads to a sufficient result, as will be shown.

In many cases it will be sufficient to just apply sequence 1. A single pre-ES, a successive IRGN will be able to identify both, the position parameters (x,y,z) and the angle parameters (ϑ, φ) successfully.

If the accuracy of the angle parameters is not yet satisfactory, then a post-ES is launched (sequence 2).

Sequence 3 has to be used if the first pre-ES supplied inappropriate starting values for the deterministic method (IRGN).

The second cycle is completely independent from the first one, however, the results are compared in the end and the results with the lower residual norm are chosen.

The results without taking data noise into account are shown in Table 5.4. It can be seen that 97% of all 100 samples (different object positions and orientations) reached the desired residual norm ε within sequence 1 while in 3 cases a second run was performed. In fact, all samples could be identified with a parameter error below 5% and the majority of samples actually reached the 1% limit. In Fig. 5.17 the success rate with respect to parameter error levels of all samples (and therefore all sequence types) are shown. It can be observed that the adaptive process becomes more important in case of noisy measurement data.

Considering noisy measurement data with a noise level of $5 \cdot 10^{-10}$, the sequence distribution

Table 5.4: Results of the hybrid identification algorithm without data noise. 100 different object positions and orientations were investigated.

	nr. of positions	mean nr. of function calls	mean error	nr. of positions		
				error $< 1\%$	error $< 2\%$	error $< 5\%$
sequ. 1	97	184	0.17	90	96	97
sequ. 2	0	-	-	-	-	-
sequ. 3	1	1 352	0.73	1	1	1
sequ. 4	2	2 246	0.97	0	0	2
sum	100	3 782	-	91	97	100

as well as the success rate changes (see Table 5.5). Again, all samples were identified with a parameter error below 5% but the number of function calls is significantly higher.

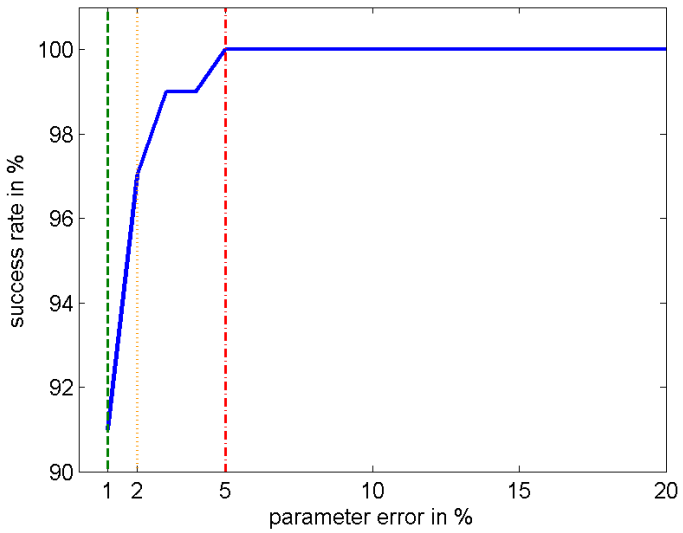

Fig. 5.17: Success rates of the hybrid identification process without data noise.

Table 5.5: Results of the hybrid identification algorithm with a data noise level of $5 \cdot 10^{-10}$. 100 different object positions and orientations were investigated.

	nr. of positions	mean nr. of function calls	mean error	nr. of positions		
				error $< 1\%$	error $< 2\%$	error $< 5\%$
sequ. 1	54	189	0.79	51	53	54
sequ. 2	1	1 026	1.02	0	0	1
sequ. 3	10	1 407	0.72	7	8	10
sequ. 4	35	2 214	1.12	27	28	35
sum	100	4 836	-	85	89	100

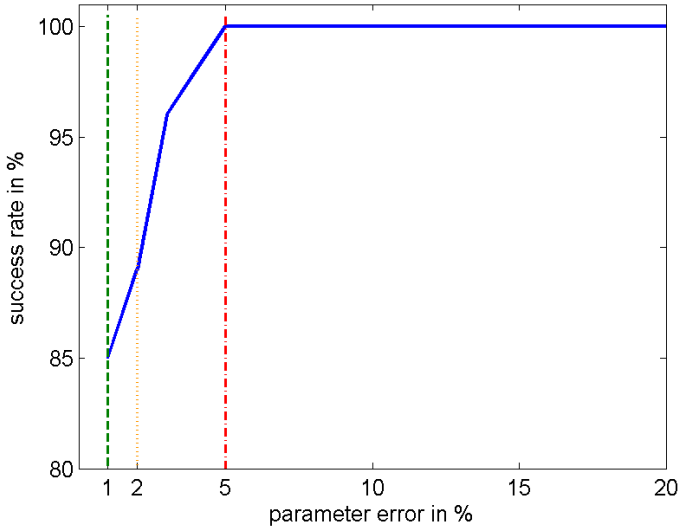

Fig. 5.18: Success rates of the hybrid identification process with a noise level of $5 \cdot 10^{-10}$.

6 Conclusion

To identify a conductive object known in shape but hidden by low- or non-conductive material, a non-destructive eddy current testing (ECT) method can be used. Preliminary works have shown that the location and orientation of an object can in principle be identified with an eddy current measurement system even if the object - sensor distance is in the range of 3 cm. This allows the design of a device able to detect the distal drill holes of a tibia nail hidden by bone and tissue. In order to identify the position of the holes exactly, a fast and accurate identification method is essential. For the sake of simplicity and to have the possibility to perform a vast number of experiments, the tibia nail was replaced by a single conductive ring.

With the help of a FEM package the eddy currents inside the ring were calculated. To minimize the computation time of the forward problem solver, a model order reduction method was found that decreases the computation time by the factor of 2 500 and provides sufficient approximation accuracy. With the simulation model the magnetic flux densities can be calculated and compared to measurement values obtained by giant magnetoresistance sensors.

To determine a measurement configuration that maps input parameter changes (position and orientation of the object) as well as possible to the output function (magnetic field values), the measurement sensitivity is of great interest. The higher the parameter sensitivity, the higher the accuracy of the identification result can be expected. It was shown that a radial configuration of the giant magnetoresistance sensors is the better choice compared to other orientations. Furthermore, it could be shown that the sensitivities of the positioning parameters x, y and z are about 4 decades higher than the angle sensitivities. Thus, identifying the angle parameters ϑ and φ is a special challenge.

When solving the inverse problem, the difference between the measured and the simulated

magnetic flux density values in a number of samples has to be minimized. An appropriate deterministic optimization method for non-linear least-squares problems is the Gauss-Newton method. Due to ill-posedness of the inverse problem, regularization is necessary. Thus, an Iteratively Regularized Gauss-Newton algorithm was used for the identification of the object position and orientation. This method is very fast and accurate even if data noise is considered. Nevertheless, the algorithm fails in some cases, especially if the initial guess (or starting value) is far away from the true solution.

Hence, a more robust stochastic optimization algorithm, namely a $(\mu/\rho, \lambda)$ Evolution Strategy, was applied. The convergence speed is much lower but the success rate is near to 100%. Nevertheless, a combination is needed to realize a fast and accurate identification algorithm. A multiple hybrid method consisting of a sequence containing a pre-Evolution Strategy, an Iteratively Regularized Gauss-Newton method and a post-Evolution Strategy was proposed. Even under noisy conditions a success rate of 100% could be achieved with a relative parameter error of below 5%.

Appendix

A.1 Calculation of the cartesian components of B produced by a conductive ring

$$\mathbf{B}(\mathbf{r}) = \frac{\mu}{4\pi} I \int_c \mathbf{e}_t \times \frac{\mathbf{r} - \mathbf{r}'}{|\mathbf{r} - \mathbf{r}'|^3} \mathrm{d}l$$

$$\mathbf{e}_t = \begin{pmatrix} -\sin\rho \\ \cos\rho \\ 0 \end{pmatrix} \quad \mathbf{r} = \begin{pmatrix} x_t \\ y_t \\ z_t \end{pmatrix} \quad \mathbf{r}' = \begin{pmatrix} R\cos\rho \\ R\sin\rho \\ 0 \end{pmatrix}$$

$$\mathbf{e}_t \times (\mathbf{r} - \mathbf{r}') = \begin{pmatrix} -\sin\rho \\ \cos\rho \\ 0 \end{pmatrix} \times \begin{pmatrix} x_t - R\cos\rho \\ y_t - R\sin\rho \\ z_t \end{pmatrix} = \begin{pmatrix} z_t\cos\rho \\ z_t\sin\rho \\ -x_t\cos\rho - y_t\sin\rho + R \end{pmatrix}$$

$$\begin{aligned} |\mathbf{r} - \mathbf{r}'|^3 &= \begin{vmatrix} x_t - R\cos\rho \\ y_t - R\sin\rho \\ z_t \end{vmatrix}^3 \\ &= \sqrt{(x_t - R\cos\rho)^2 + (y_t - R\sin\rho)^2 + z_t^2}^3 \\ &= \sqrt{(x_t^2 + y_t^2 + z_t^2 + R^2 + 2R(-x_t\cos\rho - y_t\sin\rho)}^3 \end{aligned}$$

For simplification the term $|\mathbf{r} - \mathbf{r}'|^3$ will be defined as denominator *den*. With $\mathrm{d}l = R\mathrm{d}\rho$ the

components of $\mathbf{B}(\mathbf{r})$ in cartesian coordinates can be calculated:

$$\begin{aligned}
\mathbf{B}_x(\mathbf{r}) &= \frac{\mu}{4\pi} I \int_0^{2\pi} \frac{z_t \cos\rho}{den} R \,\mathrm{d}\rho \\
\mathbf{B}_y(\mathbf{r}) &= \frac{\mu}{4\pi} I \int_0^{2\pi} \frac{z_t \sin\rho}{den} R \,\mathrm{d}\rho \\
\mathbf{B}_z(\mathbf{r}) &= \frac{\mu}{4\pi} I \int_0^{2\pi} \frac{-x_t \cos\rho - y_t \sin\rho + R}{den} R \,\mathrm{d}\rho
\end{aligned} \tag{A.1}$$

A.2 Coordinate Transformations

A.2.1 Rotation

$$\begin{pmatrix} x' \\ y' \\ z' \end{pmatrix} = \begin{bmatrix} \cos\vartheta & -\sin\varphi\sin\vartheta & \sin\vartheta\cos\varphi \\ 0 & \cos\varphi & \sin\varphi \\ -\sin\vartheta & -\cos\vartheta\sin\varphi & \cos\vartheta\cos\varphi \end{bmatrix} \begin{pmatrix} x \\ y \\ z \end{pmatrix} \tag{A.2}$$

For the calculations the ring is hold in the initial coordinate system and the test points (GMR sensors) are transformed.

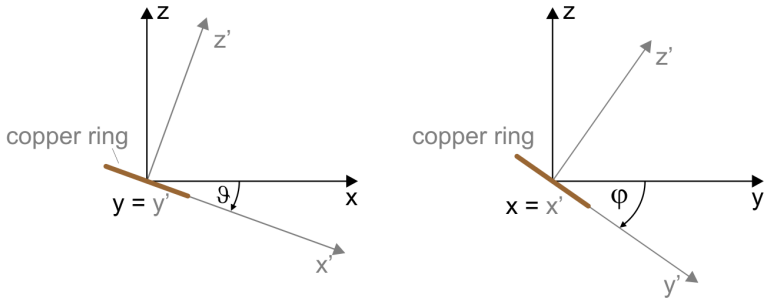

Fig. A.1: Coordinate transformation for rotation of the ring.

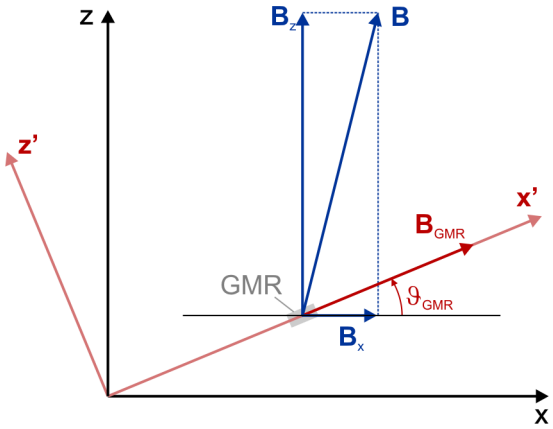

Fig. A.2: Illustration of geometry when calculating the amount of the magnetic flux density in certain direction from cartesian components of **B** (y-coordinate is neglected).

A.3 Determination of the flux density value in a certain direction

Using the rotation matrix from A.2:

$$\begin{pmatrix} B'_x \\ B'_y \\ B'_z \end{pmatrix} = \begin{bmatrix} \cos\vartheta & 0 & \sin\vartheta \\ 0 & 1 & 0 \\ -\sin\vartheta & 0 & \cos\vartheta \end{bmatrix} \begin{pmatrix} B_x \\ B_y \\ B_z \end{pmatrix} \tag{A.3}$$

Absolute value in the sensitivity axis of the GMR sensor:

$$B_{GMR} = B_x \cos\vartheta + B_z \sin\vartheta \tag{A.4}$$

Bibliography

[1] J.E. Lenz. A review of magnetic sensors. *Proceedings of the IEEE*, 78, issue 6, pp 973 - 989, 1990.

[2] Olympus Corporation. Eddy Current Array Tutorial, Depth of Penetration. *http://www.olympus-ims.com/de/ndt-tutorials/eca-tutorial/what-is-eca/depth/*.

[3] Alice Köstinger. Lokalisierung von Inhomogenitäten nicht magnetsicher Fremdkörper in humanbiologischem Gewebe unter Ausnutzung von Wirbelstromeffekten. Master's thesis, Graz University of Technology, Institute for Fundamentals and Theory in Electrical Engineering, 2005.

[4] Martin Reinbacher. Detektierung von Grenzflächen in humanbiologischem Gewebe. Master's thesis, Graz University of Technology, Institute for Fundamentals and Theory in Electrical Engineering, 2006.

[5] Markus Kienesberger. Materialinhomogenitätenerkennung durch Wirbelstromprüfung unter Verwendung von GMR-Sensoren. Master's thesis, Graz University of Technology, Institute for Fundamentals and Theory in Electrical Engineering, 2009.

[6] NVE Corporation. GMR Sensor catalog. *http://www.nve.com*.

[7] J. Hadamard. Sur les problems aux derives parielies et leur signifacation physique. *Bull. Univ. of Princton*, 1902.

[8] O. Bíró. Edge element formulations of eddy current problems. *Computer methods in applied mechanics and engineering*, 169, pp 391-405, 1999.

[9] Program tools ELEFANT, Graz, Institute for fundamentals and theory in electrical engineering, University of Technology, 2000.

[10] Mario Bellina. Eine Methode zur Positions- und Lageerkennung von Implantaten unter Ausnützung von Wirbelstromeffekten. Master's thesis, Graz University of Technology, Institute for Fundamentals and Theory in Electrical Engineering, 2011.

[11] R. Fletcher. Practical Methods of Optimization. *Wiley*, 1987.

[12] K. Levenberg. A Method for the Solution of Certain Problems in Least Squares. *Quarterly of Applied Mathematics*, 2, pp 164 168, 1944.

[13] D. Marquardt. An Algorithm for Least Squares Estimation on Nonlinear Parameters. *SIAM Journal of Applied Mathematics*, page , 11, pp 431 441, 1963.

[14] V. A. Morozov. Methods for solving incorrectly posed problems. *Springer, New York*, 1984.

[15] A. B. Bakushinskii. The problem of the convergence of the iteratively regularized Gauss Newton method. *Computational Mathematics and Mathematical Physics*, 32, pp 353 359, 1992.

[16] I. Rechenberg. Cybernetic Solution Path of an Experimental Problem. *Royal Aircraft Establishment, Library Translation No. 1122*, 1965.

[17] I. Rechenberg. Evolutionsstrategie: Optimierung technischer Systeme nach Prinzipien der biologischen Evolution. *frommann-holzboog, Stuttgart*, 1973.

[18] I. Rechenberg. Evolutionsstrategie '94. *frommann-holzboog, Stuttgart*, 1994.

[19] H. P. Schwefel. Kybernetische Evolution als Strategie der Experimentellen Forschung in der Strömungstechnik. Master's thesis, Diploma Thesis, Technical University of Berlin, 1965.

[20] H. P. Schwefel. Numerische Optimierung von Computermodellen mittels der Evolutionsstrategie. *Birkhuser Verlag*, 1977.